



DIPLOMARBEIT

Experimental and Theoretical Study of Surge in a Centrifugal Blower

ausgeführt zum Zwecke der Erlangung des akademischen Grades eines Diplom-Ingenieurs unter
der Leitung von

Ao. Univ. Prof. Dipl.-Ing. Dr. techn. Reinhard Willinger
Technische Universität Wien
Institut für Energietechnik und Thermodynamik (E302)

eingereicht an der Technischen Universität Wien, Fakultät für Maschinenwesen und
Betriebswissenschaften von

Lukas Hofmann BSc
Matrikelnummer: 1126204
Florianiweg 6, 4784 Schardenberg

Wien, am 9.Mai 2016

(Lukas Hofmann)

Preface / Danksagung

Mein vorzüglicher Dank gilt Herrn Ao. Univ. Prof. Dipl. -Ing. Dr. techn. Reinhard Willinger, der in seinen Lehrveranstaltungen mein Interesse für die thermischen Turbomaschinen weckte und mir die Möglichkeit bot, mich als studentische Hilfskraft weiter auf diesem Gebiet zu vertiefen. Ich danke ihm für die interessierte und engagierte Unterstützung beim Entstehen der vorliegenden Arbeit und für das angenehme Arbeitsklima.

Ich danke auch Roswitha Steininger sowie Michael Ludwig, die bei der Adaption des Prüfstandes wertvolle Hilfe geleistet haben.

Meinen Dank möchte ich weiters dem Betreuer meiner Bachelorarbeit, Herrn Ao. Univ. Prof. Dipl. -Ing. Dr. techn. Stefan Braun aussprechen, der scheinbar trockene Theorie für mich mit Leben erfüllte und bei meiner Diplomprüfung als Zweitprüfer zur Verfügung stand.

Mein besonderer Dank gilt meiner Familie, meiner Mutter Ute, die mich auch auf das Leben abseits der Technik nicht vergessen ließ, meinem Vater Hans, dem ich die Freude am Erforschen und Verstehen von Natur und Technik verdanke und meiner Schwester Valerie, die immer für eine Ablenkung zu haben war.

Ein Danke von Herzen auch an Magdalena, die mir immer zur Seite stand.

Kurzfassung

Die vorliegende Arbeit stellt Untersuchungen zur betrieblichen Stabilitätsgrenze (Pumpgrenze) eines am Institut für Energietechnik und Thermodynamik vorhandenen Radialgebläses an. Dabei wurden zunächst analytische Modelle angewandt, um einen Einblick in das zu erwartende Verhalten zu erlangen. Danach wurden stationäre und instationäre Messungen an Betriebspunkten nahe und jenseits der Stabilitätsgrenze durchgeführt, die erlaubten diese zu lokalisieren und das Systemverhalten im instabilen Bereich zu bestimmen. Anschließend wurden die Ergebnisse beider Ansätze verglichen und entsprechende Schlussfolgerungen gezogen.

Abstract

The thesis at hand studies the operational stability limit (surge line) of a centrifugal blower which is located at the Institute for Energy Systems and Thermodynamics. In a first step analytical models are applied to get an insight in the expected behaviour. In a second step stationary and transient measurements are performed on stable as well as unstable operational points to locate the surge line and investigate the post-surge behaviour. Finally the results of both approaches are compared and conclusions are given.

Contents

Notation	IV
1 Introduction	1
2 Theory on Compressor Stability	3
2.1 Definition of Compressor Stability	3
2.2 Stall and Surge	3
2.2.1 Stall	3
2.2.2 Surge	4
2.3 Greitzer's Lumped Parameter Model	5
2.3.1 Original Model	5
2.3.2 Overall Surge Cycle Properties and Physical Mechanism	9
2.3.3 Application to the Present Test Stand	10
2.4 Thoughts on Turbulence Intensity and RMS-Values	14
3 Measurement Technology	16
3.1 Constant Temperature Hot Wire Anemometry (CTA)	16
3.2 Temperature Sensor	18
3.3 Rotational Speed Sensor	18
3.4 Flow Rate Measurement	18
3.5 Pressure Transducer	19
3.5.1 Low Time Resolution	19
3.5.2 High Time Resolution	19
3.6 Data Acquisition System	19
4 Test Stand Configuration	20
4.1 General Notes	20
4.2 Power Converter	20
4.3 Direct Current Motor	21
4.4 Gearbox	21
4.5 Lubrication and Cooling System	22
4.5.1 Toothing Oil Supply	22
4.5.2 Bearing Oil Supply	22
4.5.3 Oil Cooling	22
4.6 Blower	22
4.6.1 General Characteristics	22

4.6.2	Impeller	24
4.6.3	Diffuser and Volute Housing	25
4.7	Orifice	25
4.8	Throttle	26
4.9	Computers	26
5	Data Analysis	27
5.1	Time-Series Analysis	27
5.1.1	Fourier Transform, Discrete Fourier Transform (DFT) and Fast Fourier Transform (FFT)	27
5.1.2	Auto and Cross Correlation	28
5.1.3	Filtering	29
5.1.4	Turbulence Intensity	29
5.2	Compressor Map Measurement	30
5.3	Inlet Flow Angle	30
6	Measurement Results	32
6.1	Compressor Map	32
6.2	Time Domain Analysis	35
6.3	Frequency Domain Analysis	38
6.4	Inlet Flow Angle	40
6.5	Turbulence Intensity	40
7	Summary and Conclusions	44
	Appendix A: Matlab Codes	47
	Appendix B: Photographies	57
	Bibliography	59

Notation

Main Symbols

Symbol	Dimension	Description
A	m^2	area
B	–	parameter
C	Pa	compressor pressure rise
C	m/s	absolute velocity spectrum
D	m	diameter
E	V	voltage
F	Pa	pressure drop across throttle
G	–	parameter
I	A	current
L	m	length
N	–	rotor revolutions
P	Pa	pressure spectrum
R	m	radius
R	$J/(kg\ K)$	specific gas constant
Re	–	Reynolds number
T	K	temperature
T	s	time period
Tu	–	turbulence intensity
V	m^3	volume
a	m/s	speed of sound
b	m	blade height

Symbol	Dimension	Description
c	m/s	absolute velocity
f	Hz	frequency
h	J/kg	specific enthalpy
j	–	imaginary unit
m	–	exponent in velocity profile
n	$1/s, rpm$	rotational speed
p	Pa	pressure
r	$m^2/s^2, Pa^2$	auto / cross correlation
t	s	time
u	m/s	circumferential velocity
w	m/s	relative velocity
Δ	–	difference
Π	–	pressure ratio
α	$^\circ, rad$	absolute flow angle
β	$^\circ, rad$	relative flow angle
δ	–	diameter number
κ	–	isentropic exponent
ν	m^2/s	kinematic viscosity
ρ	kg/m^3	density
σ	–	speed number
τ	s	compressor flow relaxation time
ψ	–	blade loading
ω	Hz	Helmholtz frequency

Subscripts

Sybscript	Description
A	armature
C	compressor, compressor duct
Or	orifice
P	plenum
RMS	root mean squared
SS	steady state
T	throttle, throttle duct
a	ambient, actual
m	mean, meridional
max	maximum
min	minimum
r	reference
s	static, isentropic
t	total
u	circumferential component
w	wire

Superscripts

Sybscript	Description
\cdot	mass or volume flow rate
\sim	dimensionless
—	mean value
$'$	fluctuating part, derivative
$+$	complementary
$*$	marking difference to similar value

Stations (except lumped parameter model)

Sybscript	Description
a	ambient
Or,1	upstream of orifice
Or,2	downstream of orifice
0	inlet duct, measuring plane
1	upstream of blading
2	downstream of blading
3	outlet blower

Chapter 1

Introduction

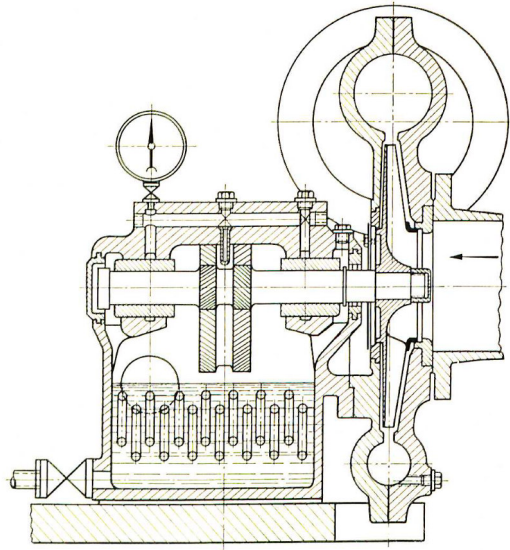
Centrifugal or radial compressors are widely in use for more than one century now. Their establishment as a standard device to deliver pressurized air for industrial applications dates back to the end of the 19th century. Nowadays this field still exhibits the most manifold scope of application for these machines.

The next significant step in centrifugal compressors' history was their use in early gas turbines as the one by Elling which delivered positive power as early as 1903. Hereinafter they have served for the turbocharging of piston engines down to the present day. The next field of application that opened up gave a strong impetus to the further development: the jet engine. Ever since von Ohain's HeW 3B engine (maiden flight 1939) and Whittle's W1 engine (maiden flight 1941) the centrifugal compressor has had its place in aeronautics. Due to its slimmer shape and greater flow capacity the axial compressor was the successful one in large aircraft propulsion, but the centrifugal one is still in use for small jet engines, shaft engines in turboprops and helicopters and as auxiliary power unit (APU) for all type of aircraft. An overview of the various applications of centrifugal compressors is presented in Fig. 1.1. A more detailed history board on this topic can be found in [11].

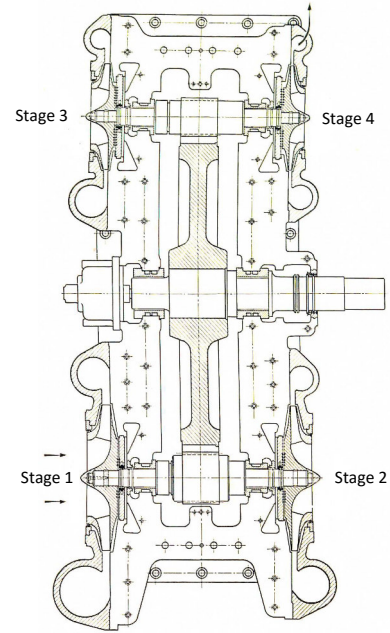
Instability phenomena referred as stall and surge have always been a common source of problems for both basic compressor types. Their prediction and detailed understanding is hard but very valuable since they limit the performance and operational points with best efficiency and highest pressure rise are usually located quite close to the stability line. Thus, on the one hand it is desirable to obtain models that are able to give a good prediction of the stability characteristics during the design process. On the other hand there is an interest for models that can serve as a basis for control systems that enlarge the operational range and improve safety. Models for the design process can be quite complex and are aimed at a comprehensive flow analysis while models for the second purpose have to be rather simple and focused on the overall system behaviour as they have to give fast input to the controller based on little information.

Since a better understanding of unstable behaviour promises considerable benefits a lot of effort has been put in both of the mentioned approaches but it can be observed that stall and surge is much less well explained in radial compressors than in axial ones (see [4, p. 364f]). This may have several reasons as the comparably complex flow regime in centrifugal compressors but also less research due to their higher tolerance to stalled regions or the observation that the optimum operational point is usually not that close to the surge line as in axial compressors (see [2, p.1109]).

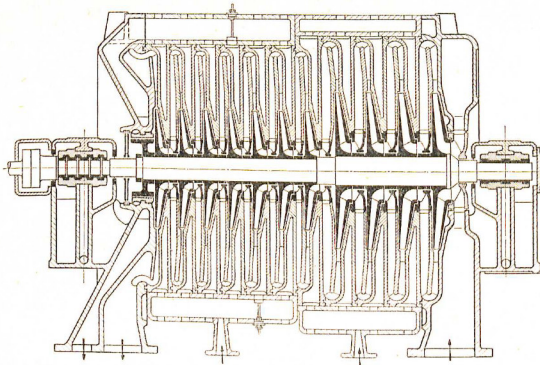
However, the present study wants to make a modest contribution to this wide and interesting



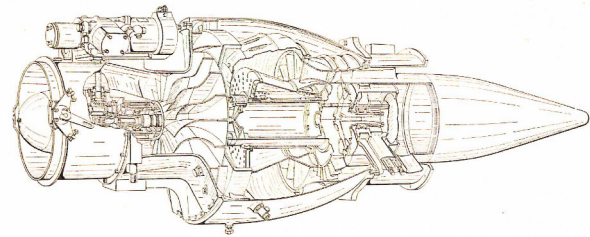
(a) DEMAG Industrial blower



(b) DEMAG 4-stage geared compressor



(c) DEMAG 11-stage compressor



(d) Turboméca Mariboré II jet engine

Figure 1.1: Illustration of the various applications for centrifugal compressors, all figures taken from [6].

field of research. It is needless to say that the limited scope of a diploma thesis and the university's infrastructural and personnel situation inhibit extensive measurements and simulations. Hence, I got – also during my activities as a laboratory assistant – a little insight in the daily routine of academic research or the art of the possible.

Although it was tried to avoid inconsistencies in nomenclature some symbols will have a different meaning in different contexts. Otherwise unusual denominations would have been necessary which would not have improved readability and as R. W. Emerson said, a foolish consistency is the hobgoblin of little minds.

Chapter 2

Theory on Compressor Stability

2.1 Definition of Compressor Stability

The stability of a state can generally be defined as the immunity to small perturbations. In the context of compressors two basic types of stability can be identified: operational or static stability and aerodynamic or dynamic stability. The first one is determined by the matching of the compressor characteristic and the throttle line. Stable operation is given as long as the slope of the throttle line is greater than the slope of the compressor characteristic in the operational point. For a stable point a small increase of the flow rate leads to a decrease of the pressure rise whereby the original equilibrium will be restored. An analogous consideration can be made for a small shift to a lower flow rate. If this criterion is violated a higher flow rate leads to a higher pressure rise and the other way round which drives operation away from the original point .

This simple approach cannot explain all instability phenomena that occur in real machines. Therefore, one has to consider a second type of stability. If steady state operation cannot be established although the static stability criterion is satisfied aerodynamic or dynamic instability is the reason. Often it is this harder to predict kind of instability which limits the operational range due to stall and surge (see [4, p. 359f], [6, p. 477f], [10, p. 194ff], [14, p. 1-4 ff]) . The thesis at hand deals with this field of instability.

2.2 Stall and Surge

2.2.1 Stall

In the theory of airfoils stall means that the boundary layer is separating since it is not able to withstand a certain pressure rise. For a given airfoil the onset of this phenomenon is usually dependent on the angle of attack and to a lesser extent on the Reynolds number.

With turbomachinery or with compressors in particular the situation is a bit different from the single airfoil in an undisturbed external flow. The most obvious difference is the fact that multiple airfoils or blades are used in each row. Another major difference is that in multi-stage machines every row downstream the first one is facing an inhomogeneous flow. One can also mention the higher effect of the walls with their associated boundary layers and the effect of tip clearance in rotating rows.

Now in the context of compressors one can identify two types of stall. The first one is individual stall which would be expected assuming identical blades and a homogeneous flow. It

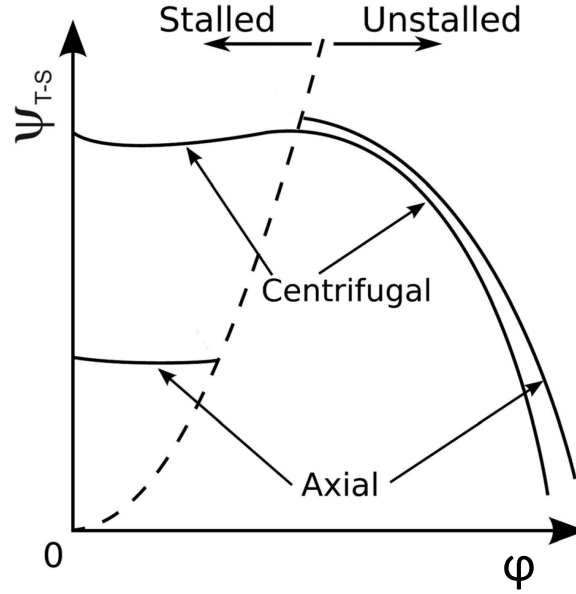


Figure 2.1: Illustration of the pressure drop in axial and radial compressors in the presence of stall; figure taken from [5, p. 6] and adapted; for definitions of ψ and φ see below.

occurs when the entire blade row stalls at once. Due to deviations from the ideal assumptions mentioned above the most common type of stall is rotating stall where just a few blades are stalled at once. There may be one or several stall cells rotating in the same direction as the rotor at some fraction of its rotational speed. These cells may extend right across the annulus (known as full-span stall) or just cover a part of its height (known as part-span stall).

However, rotating stall always leads to a drop in pressure rise at a given flow. As presented in Fig. 2.1 axial compressors typically exhibit a rotating stall featuring a large drop in pressure rise and flow (so called abrupt or deep stall) while centrifugal ones usually experience just an inappreciable drop in overall performance (so called progressive or mild stall).

This is because much of the pressure rise is produced by centrifugal forces which have an effect on a separated flow too. Thus, it is often feasible to operate in a satisfactory way even with rotating stall present (see [4, p. 364ff]). This may be the cause that the greatest research effort has been with stall of axial compressors.

2.2.2 Surge

In case of surge the whole compression system is unstable. This flow state is characterized by fluctuations of the average flow through the compressor as well as of the pressure rise. This results in a so called surge cycle which is presented in an idealized version in Fig. 2.3. In surge operation the system is unable to attain a stable operational point (see Fig. 2.2). The loading and unloading of the compression system lead to heavy transient mechanical loads. Compared to rotating stall the time scale for surge is longer and in contrast to stall it is determined by the time to fill and empty the storage volume not the flow pattern in and around the compressor (see [4, p. 361]). Typical frequencies of pressure and velocity fluctuations caused by surge are $5 \div 10 \text{ Hz}$ while stall leads to one order of magnitude greater dominant frequencies of about $50 \div$

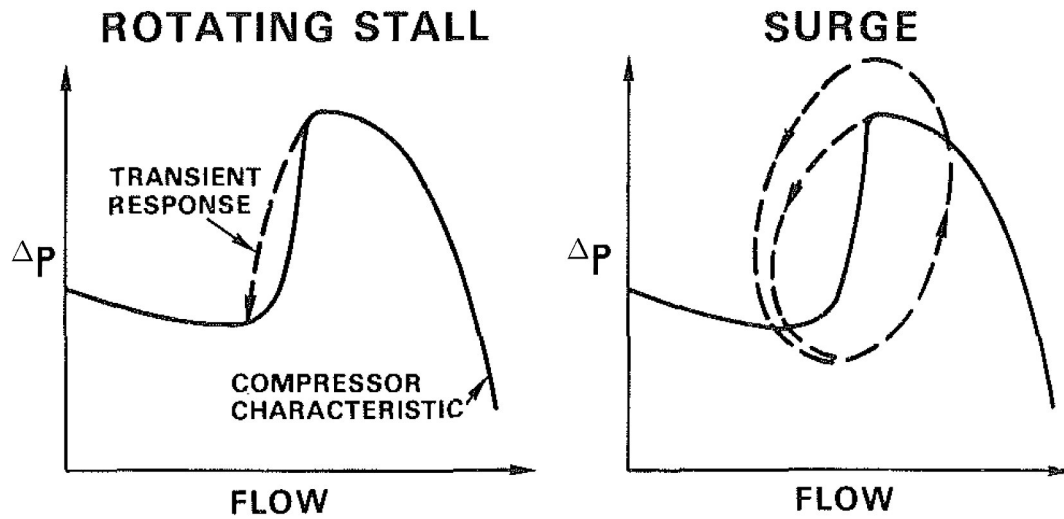


Figure 2.2: Transient system response subsequent to initial instability; figure taken from [10, p. 205] and adapted.

100 Hz . Similar to stall one can distinguish between mild and deep or violent surge depending on its intensity. Unlike stall surge is a one-dimensional phenomenon which simplifies its detection and analysis.

In [7] eight parameters have been identified which effect the surging of centrifugal compressors:

- Gradient of compressor pressure rise characteristic and the limited aerodynamic performance range of each component
- Inducer incidence
- Impeller blade backsweep
- Inlet swirl
- Number of diffuser and impeller vanes
- Pressure recovery within the semivaneless-space (SVS) and incidence on the diffuser vane leading edge
- Diffuser channel pressure recovery and collector type
- Casing treatments

To discuss them would go beyond the scope of this work but this listing can be a guidance in the design process when considering the surge issue.

2.3 Greitzer's Lumped Parameter Model

2.3.1 Original Model

In 1976 Greitzer (see [9]) offered a system instability model for axial flow compressors based on system component characteristics which allows to predict whether a certain configuration will

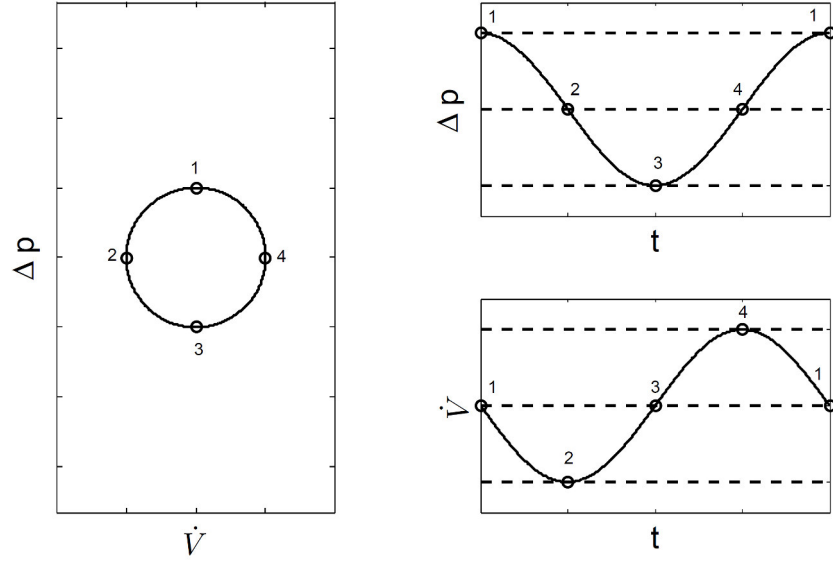


Figure 2.3: Idealized surge cycle, illustrating a phase shift of a quarter period between pressure rise and flow rate.

exhibit stall or surge and what the transient behaviour will look like. Although Greitzer's theory was developed for axial compressors it turned out to be suitable for centrifugal compressors too when using a smaller relaxation time (see below) as has been reported by Hansen et al. (see [8, p. 394]).

The equivalent compression system used in the described model is illustrated in Fig. 2.4. One can formulate the equation of motion for the duct between compressor and plenum for an incompressible flow as

$$p_{2t} = p_{Pt} + \rho \int_0^{L_C} \frac{dc}{dt} ds. \quad (2.1)$$

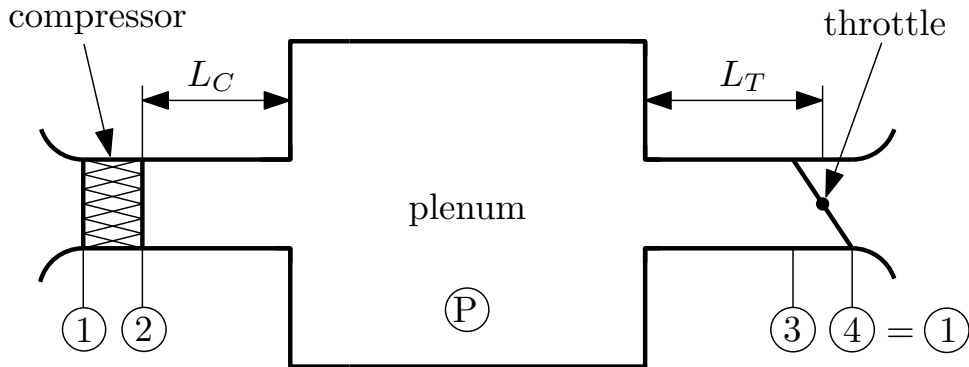


Figure 2.4: Equivalent compression system used by Greitzer.

After integrating the last term this equation can be rearranged as follows:

$$\begin{aligned}
 \frac{dc}{dt} L_C \rho A_C &= (p_{2t} - p_{Pt}) A_C \\
 &= (-\underbrace{(p_{Pt} - p_{1t})}_{\Delta p} + \underbrace{(p_{2t} - p_{1t})}_C) A_C \\
 &= (-\Delta p + C) A_C .
 \end{aligned} \tag{2.2}$$

Using the same scheme for the duct between plenum and throttle one arrives at

$$\begin{aligned}
 \frac{dc}{dt} L_T \rho A_T &= (\underbrace{(p_{Pt} - p_{1t})}_{\Delta p} - \underbrace{(p_{3t} - p_{1t})}_F) A_T \\
 &= (\Delta p - F) A_T .
 \end{aligned} \tag{2.3}$$

Assuming incompressible flow the derivative of mass flow with respect to time is just a function of the change in velocity which reads

$$\frac{d\dot{m}}{dt} = \frac{dc}{dt} \rho A. \tag{2.4}$$

Using this relation Eq. (2.2) and Eq. (2.3) can be modified to

$$\frac{d\dot{m}_C}{dt} \frac{L_C}{A_C} = -\Delta p + C \tag{2.5}$$

and

$$\frac{d\dot{m}_T}{dt} \frac{L_T}{A_T} = \Delta p - F. \tag{2.6}$$

As a next step it seems legit to assume that the pressure drop across the throttle is equal to the dynamic pressure at the discharge plane. This allows to find for F the relation

$$F = \frac{1}{2} \rho c_{T,a}^2 = \frac{1}{2} \rho c_{T,a}^2 \frac{\rho A_{T,a}^2}{\rho A_{T,a}^2} = \frac{\dot{m}_T^2}{2 \rho A_{T,a}^2}. \tag{2.7}$$

Note that $c_{T,a}$ and $A_{T,a}$ refer to the discharge plane. For a variable area nozzle or a valve this means that $A_{T,a}$ is the manipulated variable. It is not the fixed duct area A_T . Then Eq. (2.6) finally becomes

$$\frac{d\dot{m}_T}{dt} \frac{L_T}{A_T} = \Delta p - \frac{\dot{m}_T^2}{2 \rho A_T^2}. \tag{2.8}$$

Mass conservation for the plenum is given by

$$\dot{m}_C - \dot{m}_T = V_P \frac{d\rho}{dt} \tag{2.9}$$

since the plenum volume is constant. To substitute the time derivative of the density it is assumed that the thermodynamic process in the plenum is isentropic which allows to use

$$p_P \left(\frac{1}{\rho_P} \right)^\kappa = \text{constant}. \tag{2.10}$$

Note that the velocity in the plenum is negligible ($p_{Pt} = p_P$). After differentiation and rearranging one gets

$$\frac{d\rho_P}{dt} = \frac{\rho_P}{\kappa p_P} \frac{dp_P}{dt}. \quad (2.11)$$

Additionally it is assumed that ρ_P/p_P is nearly the same as ρ_a/p_a which is justified by the condition that the pressure and temperature ratio of the compression system are near unity. Then the mass conservation in the plenum is

$$\dot{m}_C - \dot{m}_T = V_P \frac{\rho}{\kappa p} \frac{dp_P}{dt}. \quad (2.12)$$

When reaching the stall limit line the compressor does not respond quasi-steadily to changes in mass flow. Actually a finite amount of time (usually several rotor revolutions) is needed to establish a fully developed rotating stall pattern. This fact is simulated by

$$\tau \frac{dC}{dt} = C_{SS} - C, \quad (2.13)$$

where C_{SS} is the steady state pressure rise and τ is the relaxation time which has to be determined by measurements respectively estimated based on the compressor's geometry. Generally it is different for axial and radial machines as said above. Greitzer expresses this relaxation time as a function of the number of revolutions needed for stall development which reads

$$\tau = N \frac{2\pi R_2}{u_2}. \quad (2.14)$$

The system is fully described by the Eq. (2.5), (2.8), (2.6), (2.13) and (2.7). These equations can now be expressed nondimensionally. The following equations introduce dimensionless variables in place of the dimensioned variables:

$$\dot{\tilde{m}} = \frac{\dot{m}}{\rho u_2 A_C}, \quad \tilde{p} = \frac{p}{\frac{1}{2} \rho u_2^2}, \quad \tilde{t} = t\omega, \quad \tilde{\tau} = \frac{2\pi N R_2 \omega}{u_2}. \quad (2.15)$$

The Helmholtz frequency ω which is given by

$$\omega = a \sqrt{\frac{A_C}{L_C V_P}} \quad (2.16)$$

is the natural frequency of the duct-plenum system without compressor and throttle. The speed of sound a for an ideal gas is

$$a = \sqrt{\kappa R T}. \quad (2.17)$$

In dimensionless form the system equations from above become

$$\frac{d\dot{\tilde{m}}_C}{d\tilde{t}} = B(\tilde{C} - \Delta\tilde{p}), \quad (2.18)$$

$$\frac{d\dot{\tilde{m}}_T}{d\tilde{t}} = \frac{B}{G} (\Delta\tilde{p} - \tilde{F}), \quad (2.19)$$

$$\frac{d\Delta\tilde{p}}{d\tilde{t}} = \frac{1}{\tilde{B}} (\dot{\tilde{m}}_C - \dot{\tilde{m}}_T), \quad (2.20)$$

$$\frac{d\tilde{C}}{d\tilde{t}} = \left(\frac{1}{\tilde{\tau}}\right) (\tilde{C}_{SS} - \tilde{C}). \quad (2.21)$$

In these equations the now famous B parameter is

$$B = \frac{u_2}{2a} \sqrt{\frac{V_P}{A_C L_C}} \sim \frac{\text{pressure forces}}{\text{inertial forces}}. \quad (2.22)$$

As indicated it gives a relation between pressure forces and inertial forces (see [5, p.6f]). If pressure forces are dominant, the system will exhibit surge behaviour. If inertia forces are dominant instead the compressor will just experience rotating stall. Thus, it is possible to determine a critical value of B demarcating surge from stall behaviour for a given compressor. To make the physical significance clearer the parameter can be rewritten as

$$B = \frac{(\rho u_2^2/2) A_C}{\rho u_2 \omega L_C A_C}. \quad (2.23)$$

The numerator is a value proportioned to the compressor's pressure rise capability multiplied by the duct area. It represents the driving force for the acceleration of the fluid in the duct. The denominator contains the product $\rho L_C A_C$ which is the mass in the duct. The axial velocity c is approximately proportional to U . This means that the denominator is proportional to $\rho c \omega L_C A_C$ which gives the force which is required to produce small flow oscillations in the duct or in other words to overcome the fluid's inertia (see [4, p.392f] and [10, p.205]).

The second parameter G which appears to have just minor influence on the system behaviour is given by

$$G = \frac{A_C L_T}{A_T L_C}. \quad (2.24)$$

2.3.2 Overall Surge Cycle Properties and Physical Mechanism

In order to analytically examine the overall surge properties it is useful to consider a simpler model. Greitzer carries out an analysis with the same aim in [9, p.196f]. A very economic and quite intuitive treatment has been applied by Stenning in [17, p.18f] which served as a basis for the following considerations. To reduce complexity of the more general model above the inertia forces in the throttle duct are neglected. This means

$$\Delta p = F. \quad (2.25)$$

Therefore, Eq.(2.6) respectively (2.8) is satisfied identically. Furthermore, the compressor response is taken to be quasi-steady. This makes Eq.2.13 obsolete. Introducing the linear relations

$$\dot{m} = \bar{\dot{m}} + \delta \dot{m}, \quad (2.26)$$

$$\Delta p = \bar{\Delta p} + \left(\frac{d\bar{\Delta p}}{d\dot{m}_T}\right) \delta \dot{m}_T = \bar{F} + \bar{F}' \delta \dot{m}_T, \quad (2.27)$$

$$C = C_{SS} = \bar{C}_{SS} + \left(\frac{d\bar{C}_{SS}}{d\dot{m}_C}\right) \delta \dot{m}_C = \bar{C}_{SS} + \bar{C}'_{SS} \delta \dot{m}_C, \quad (2.28)$$

for small perturbations and using the identity

$$\bar{C}_{SS} = \bar{F} \quad (2.29)$$

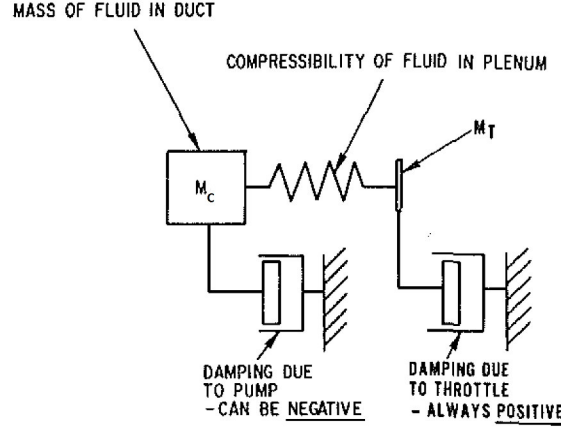


Figure 2.5: The mechanical analogue of the compression system; the damping due to the throttle has been neglected for the linearized analysis; taken and adapted from [10, p. 196].

one arrives at the equation system

$$\frac{d\delta\dot{m}_C}{dt} \frac{L_C}{A_C} = \overline{C}'_{SS} \delta\dot{m}_C - \overline{F}' \delta\dot{m}_T, \quad (2.30)$$

$$\frac{d\delta\dot{m}_T}{dt} \overline{F}' V_P \frac{\rho}{\kappa p} = \delta\dot{m}_C - \delta\dot{m}_T. \quad (2.31)$$

These two equations can be reduced to one single second order ordinary differential equation by eliminating either $\delta\dot{m}_C$ or $\delta\dot{m}_T$ as follows:

$$\frac{d^2 \delta\dot{m}_C}{dt^2} \frac{\overline{F}' L_C V_P \rho}{A_C p \kappa} + \frac{d\delta\dot{m}_C}{dt} \left(\frac{L_C}{A_C} - \frac{\overline{C}'_{SS} \overline{F}' V_P \rho}{p \kappa} \right) + \delta\dot{m}_C (\overline{F}' - \overline{C}'_{SS}) = 0. \quad (2.32)$$

This equation has constant coefficients if the disturbances are small. The analogy to a mechanical system as presented in Fig. 2.5 is obvious. The coefficient of $\frac{d^2 \delta\dot{m}_C}{dt^2}$ is always positive for any real valve. Now there are two possibilities for unstable behaviour. The first one is that the coefficient of $\delta\dot{m}_C$ is negative which means that the slope of the compressor characteristic is steeper than that of the throttle line. This situation has already been identified as static instability. In the analogue this means a negative spring rate. The second possibility is that the coefficient of $\frac{d\delta\dot{m}_C}{dt}$ becomes negative. In this case the system is dynamically unstable and will experience surge. This corresponds to negative damping in the analogue.

2.3.3 Application to the Present Test Stand

It was not possible to realize a test stand configuration as used by Greitzer and Stenning. Hence, the model above can just be applied to a fictive test stand. Nevertheless, this theoretical approach allows to get an idea of the instability characteristics.

At first the static instability criterion shall be evaluated. Therefore, we consider the lowest measured flow rate for each rotational speed (see Fig. 6.1). Assuming that \overline{F} can be approximated by

$$\overline{F} = k \overline{\dot{m}}_T^2 = k \overline{\dot{m}}^2. \quad (2.33)$$

n [rpm]	\dot{V}_{min} [m^3/s]	$\bar{F} = \Delta\bar{p} = \bar{C}_{SS}$ [Pa]	k [($m\ kg$) $^{-1}$]	\bar{F}' [Pa s/kg]	\bar{C}'_{SS} [Pa s/kg]
3000	0.078	2353	273570	50743	2535
4000	0.155	4229	124512	45894	2367
5000	0.191	6405	124191	56407	2618

Table 2.1: Values for the evaluation of the static stability criterion; * calculated from derivative of curve fit of compressor characteristics (see Tab. 6.1).

the values in Tab. 2.1 can be calculated for each operational point when additionally assuming a density. For the given values a density of $\rho = 1.189 \frac{kg}{m^3}$ was used. In fact this very coefficient has qualitatively no influence on the result. It is obvious that for none of these points $\bar{C}'_{SS} \geq \bar{F}'$ which means that they are statically stable. This criterion is fully valid also for the test stand in chapter 4 since only the throttle line and the compressor map are germane here. The criterion for static instability is

$$\bar{C}'_{SS} \geq \frac{p\kappa L_C}{A_C V_P \rho} \frac{1}{\bar{F}'} . \quad (2.34)$$

To make an evaluation possible the following numerical values have been inserted (density as above):

$$A_C = 0.09898\ m^2, \quad L_C = 7\ m, \quad p = 1013\ hPa, \quad \kappa = 1.4. \quad (2.35)$$

The polynomial representation of the compressor characteristics is given in section 6.1. For the linearized analysis the representation of the full characteristic has been used. Note that strictly the total-to-total characteristic has to be used but for the given configuration with almost equal inlet and outlet diameters the maximum difference from static to total pressure rise is below $2\ Pa$ which is definitely below the uncertainty of the measurement.

The results for two different plenum volumes in Tab. 2.2 and 2.3 and their comparison to Tab. 2.1 clearly reveal some trends. The dynamic stability criterion is usually the one which is violated first. Another observation that can already be made in Eq. (2.34) is that the onset of dynamic instability is always located on the positively sloped side of the characteristic. A greater plenum volume shifts this point towards the maximum pressure rise. Consequently there is no such thing as one single surge line for a given machine. It always depends on the configuration of the whole system.

To get an insight into the post-surge behaviour the assumption of small perturbations is no longer valid. This means that the full first order ordinary differential equation system from above has to be solved for each time step. In order to achieve the same order of magnitude of pressure rise and mass flow the dimensionless equations have been used. This made a functional representation of the dimensionless compressor map necessary which is given in section 6.1. Note that the unstable branch of the characteristics near zero mass flow is just an estimation since it could not be measured. Without this artificial part no stable surge cycle for great plenum volumes could be achieved. Note that for the full analysis some measured operational point corresponding to high mass flows have not been included in the determination of the polynomial fit.

n [rpm]	\dot{V}_{min} [m^3/s]	$\bar{F} = \Delta\bar{p} = \bar{C}_{SS}$ [Pa]	k [($m\ kg$) $^{-1}$]	\bar{F}' [Pa s/kg]	\bar{C}'_{SS}^* [Pa s/kg]
3000	0.1603	2449	67408	25696	33.1
4000	0.2194	4305	63265	33005	25.5
5000	0.2771	6514	60008	39540	21.2

Table 2.2: Values at the operational point at which the dynamic stability criterion is violated first; $V_P = 10\ m^3$; * calculated from derivative of curve fit of compressor characteristics (see Tab. 6.1).

n [rpm]	\dot{V}_{min} [m^3/s]	$\bar{F} = \Delta\bar{p} = \bar{C}_{SS}$ [Pa]	k [($m\ kg$) $^{-1}$]	\bar{F}' [Pa s/kg]	\bar{C}'_{SS}^* [Pa s/kg]
3000	0.1207	2431	118080	33883	830.0
4000	0.1923	4293	82069	37540	749.0
5000	0.2473	6503	75220	44232	635.7

Table 2.3: Values at the operational point at which the dynamic stability criterion is violated first; $V_P = 0.3\ m^3$; * calculated from derivative of curve fit of compressor characteristics (see Tab. 6.1).

Besides geometry and the compressor map representation the input values are the density, the rotational speed, the parameter N , the initial mass flow rate and the the throttle setting which is described by \tilde{k} . This is because the pressure drop across the throttle has been modelled analogue to the linearized analysis as

$$\tilde{F} = \tilde{k} \dot{m}_T^2. \quad (2.36)$$

The Matlab codes used can be found in Appendix A. They have been validated by comparison to simulation results given in [8] and [12]. The simulation for the given blower gives qualitatively realistic results (see Fig. 2.6 and Fig. 2.7). For both of them the simulated time period was 10 s. As expected the critical throttle settings represent operational points on the positively sloped part of the characteristic.

It has to be emphasized that the surge behaviour and its onset are influenced by the geometry parameters which have been chosen arbitrarily. Thus, the surge line and the surge cycle will look different for different configurations.

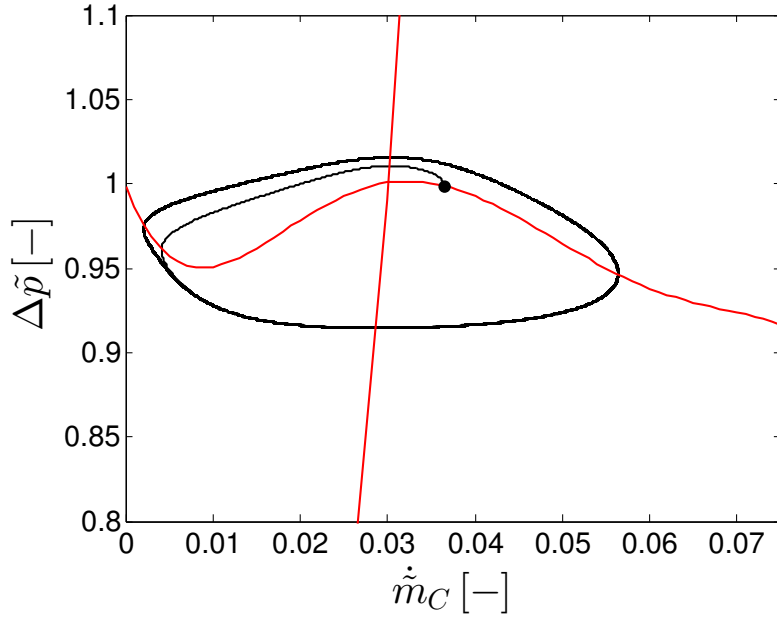


Figure 2.6: Simulated surge cycle for $n = 5000rpm$, $N = 0.5$, $L_C = 7m$, $L_T = 3m$, $\dot{m}_{C,initial} = \dot{m}_{T,initial} = 0.45kg/s$, $D_C = D_T = 0.355m$, $\rho = 1.189kg/m^3$, $a = 340m/s$, $V_P = 10m^3$, $\tilde{k} = 1100$; dot represents the initial operational point.

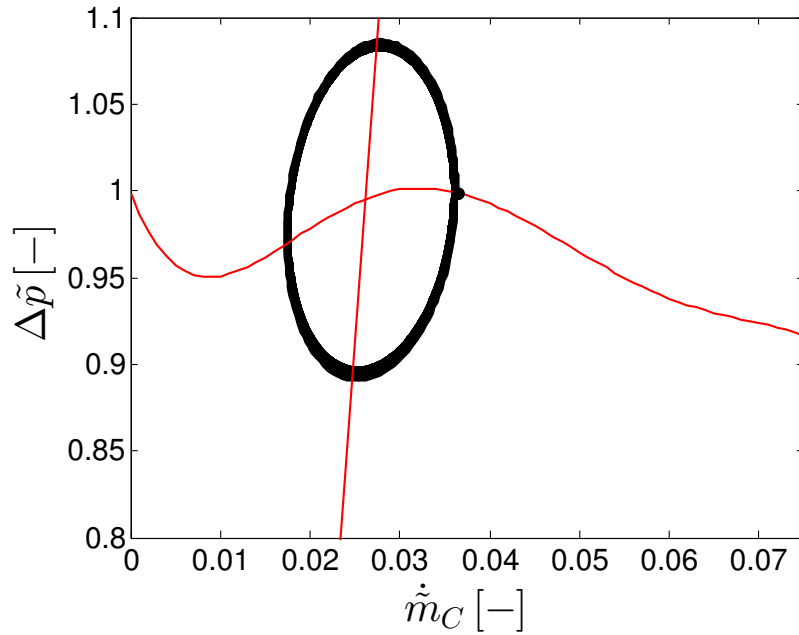


Figure 2.7: Simulated surge cycle for $n = 5000rpm$, $N = 0.5$, $L_C = 7m$, $L_T = 3m$, $\dot{m}_{C,initial} = \dot{m}_{T,initial} = 0.45kg/s$, $D_C = D_T = 0.355m$, $\rho = 1.189kg/m^3$, $a = 340m/s$, $V_P = 0.3m^3$, $\tilde{k} = 1400$; dot represents the initial operational point.

2.4 Thoughts on Turbulence Intensity and RMS-Values

In the preliminary stages of this thesis a first motivation was achieved by some simple thoughts concerning the coherence of the turbulence intensity Tu_0 , the flow coefficient φ^* and root-mean-square (RMS) values of the pressure signal when approaching the surge line. Assuming incompressible flow one can use the Bernoulli equation for defining the total pressure p_t which leads to

$$p_t = p + \frac{\rho c^2}{2}. \quad (2.37)$$

Introducing a separation between mean values which are marked with a bar ($\bar{}$) and fluctuating parts marked with a dash ($'$) one can achieve

$$\bar{p}_t + p'_t = \bar{p} + p' + \frac{\rho (\bar{c} + c')^2}{2}. \quad (2.38)$$

After averaging in time one ends up at

$$\bar{p}_t = \bar{p} + \underbrace{\frac{\rho \bar{c'^2}}{2}}_{p_{RMS}} + \frac{\rho \bar{c}^2}{2}. \quad (2.39)$$

Furthermore, the flow coefficient φ^* and the turbulence intensity Tu for isotropic turbulence (see section 5.1.4) are defined by

$$\varphi^* = \frac{\bar{c}_0}{u_2} \quad (2.40)$$

and

$$Tu = \frac{\sqrt{\bar{c'^2}}}{\bar{c}}. \quad (2.41)$$

Rearranging some terms and introducing these two dimensionless numbers the wanted relation can be found:

$$\frac{p_{0,RMS}}{\rho u_2^2} = \frac{1}{2} \frac{\bar{c'^2}}{u_2^2} = \frac{1}{2} \frac{\bar{c'^2}}{\bar{c}_0^2} \frac{\bar{c}_0^2}{u_2^2} = \frac{1}{2} Tu_0^2 \varphi^{*2}. \quad (2.42)$$

Treating this as a valid equation one would expect p_{RMS} to decrease monotonously when throttling. As presented in Fig. 2.8 this is not the case. Obviously none of the phenomena stall or surge have been taken into consideration. Thus, a qualitatively different behaviour can be an indication of system instability. An unknown quantity in this context is Tu . It can just be predicted based on measured pressure RMS values. In order to compare measurements to this simple model (see section 6.5) the equation above has to be rearranged to

$$Tu_0 = \sqrt{\frac{2 p_{0,RMS}}{\rho u_2^2 \varphi^{*2}}}. \quad (2.43)$$

The turbulence intensity predicted by this model is not realistic of course but it can still be a good approximation for the qualitative behaviour (see Fig 2.9). Whether or not this is the case will be discussed in section 6.5.

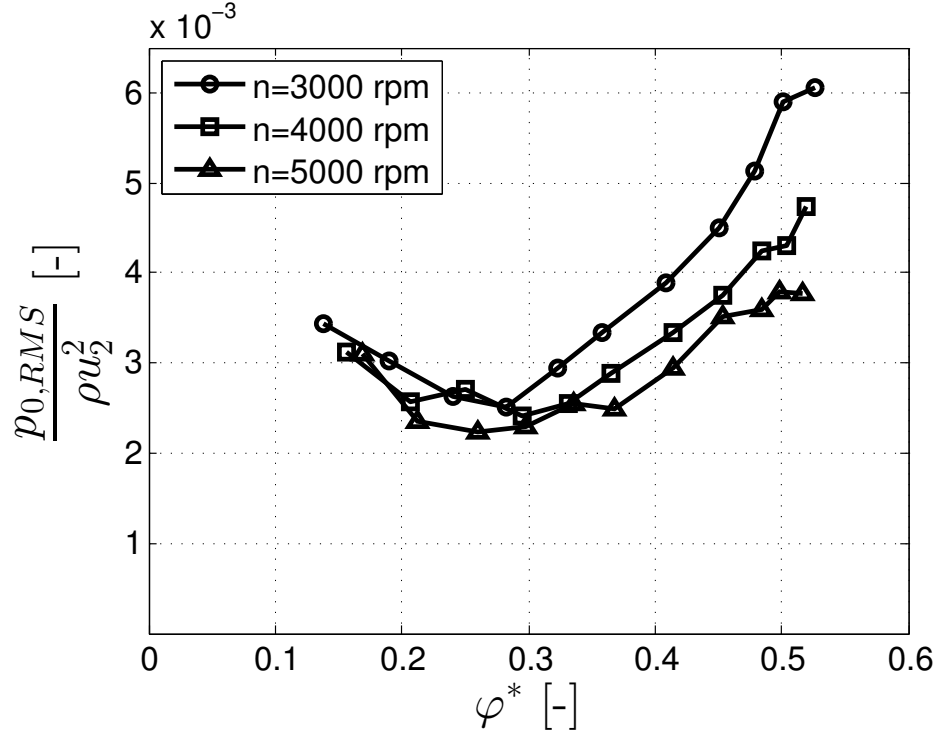


Figure 2.8: RMS deviations of the slow piezoresistive inlet pressure measuring.

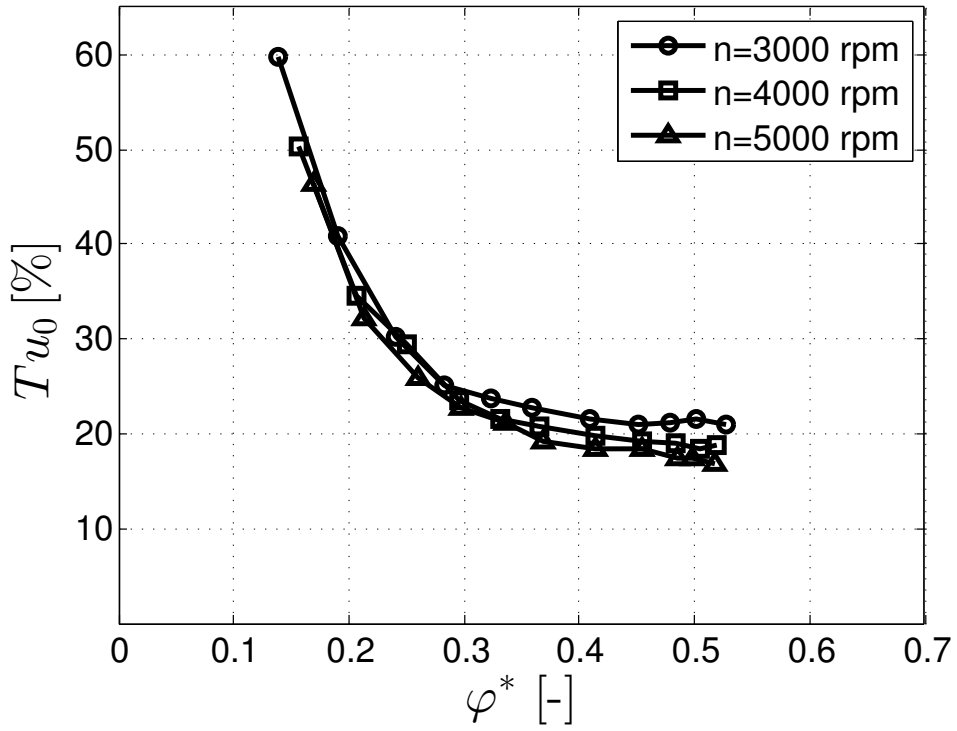


Figure 2.9: Turbulence intensity (b) predicted according to Eq. (2.43).

Chapter 3

Measurement Technology

3.1 Constant Temperature Hot Wire Anemometry (CTA)

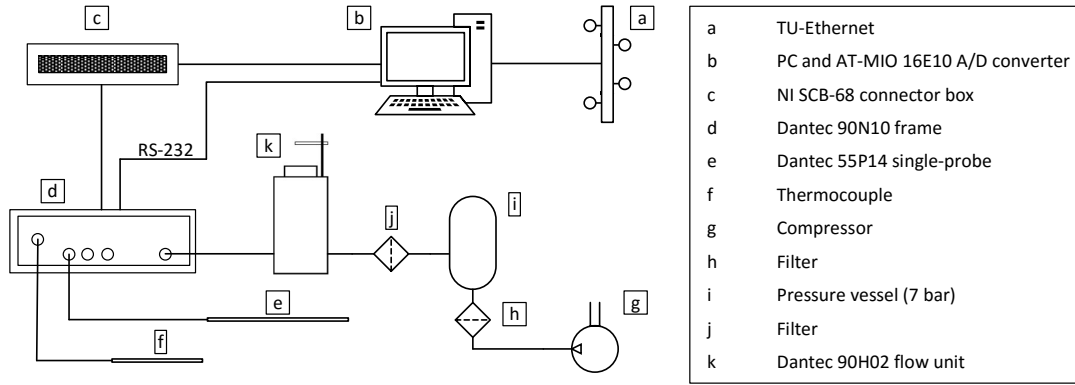


Figure 3.1: Configuration of the CTA system.

The overall configuration of the CTA measurement equipment is presented in Fig. 3.1. In CTA a hot wire with a diameter of just a few μm is being cooled by the studied flow. The voltage needed to keep the wire's temperature constant is proportional to the flow velocity's magnitude. Because of its small dimensions the wire's thermal inertia is vanishingly low which allows very high time resolutions even able to measure turbulent fluctuations. For the thesis at hand a DANTEC 55P14 single probe was used (see Fig. 3.2). This probe allows one-dimensional measurements which is sufficient for the present purpose. The measuring plane of this probe is perpendicular to the probes axis since it is meant to be in the main flow direction. The length of this probe's wire is $1.25mm$ and its diameter is $5\mu m$.

The traditional calibration equation for single normal probes based on history and physical considerations is defined as a power law (see [3, p.95f]) which reads

$$E^2 = A + B c^n \quad (3.1)$$

with E as measured voltage. This equation is valid for a comparably small Reynolds number range. Furthermore an inversion has to be done to derive the flow velocity from a measured voltage. Out of these reasons a polynomial fit of the form

$$c = C_5 + C_4 E + C_3 E^2 + C_2 E^3 + C_1 E^4. \quad (3.2)$$

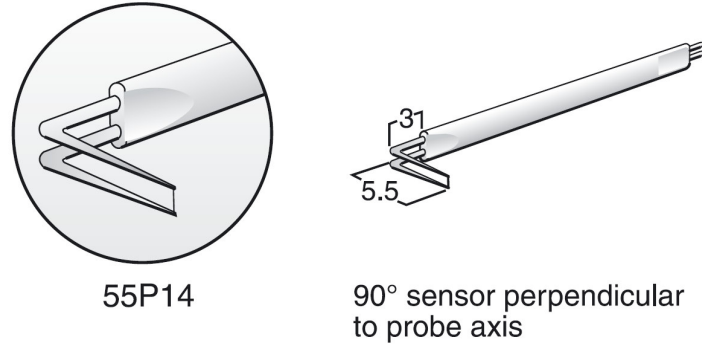


Figure 3.2: DANTEC CTA single probe 55P14, figure taken from the DANTEC Dynamics catalogue "Probes for Hot-wire Anemometry".

has been used (see Fig.3.3 and [3, p.98f]). Such curve fits tend to oscillate when measuring velocities outside the calibration band but for the given task it could be ensured that none of the measured velocities exceeds those limits.

In order to avoid effects caused by temperature changes in the medium the probe is equipped with a thermocouple which allows automatic temperature compensation. For its functional principle see the next section. The temperature compensation is implemented as

$$E_{korrr} = E \left(\frac{T_w - T_r}{T_w - T_a} \right)^{0.5}, \quad (3.3)$$

where T_w stands for the wire temperature, T_r for the reference temperature and T_a for the actual flow temperature.

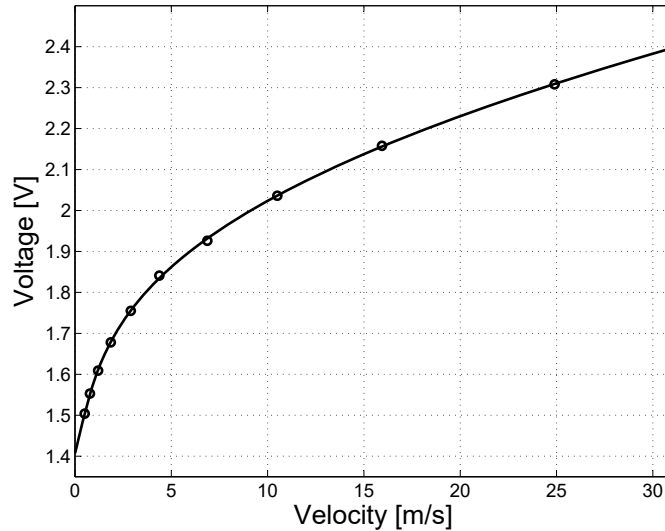


Figure 3.3: Calibration curve of the 55P14 hot-wire probe at reference temperature, fitted with a fourth-order-polynomial.

Because of the low flow velocities at maximum throttle closing it has to be taken into consideration that the assumption of pure forced-convection heat transfer may no longer be valid (see [3, p.105ff]). Therefore, the wire Reynolds number at the lowest occurring velocity has to be calculated, which is

$$Re_{w,min} = \frac{c d_w}{\nu} \approx \frac{1.5 \cdot 5 \cdot 10^{-6}}{160 \cdot 10^{-7}} = 0.4687. \quad (3.4)$$

This value is greater than the critical wire Reynolds number which is usually not higher than 0.1. Hence, the assumption of pure forced-convection heat transfer is justified for the measurements performed.

3.2 Temperature Sensor

For the temperature measurements at the blower's inlet (station 0) and outlet (station 3) two Pt100 platin resistance thermometers manufactured by Testo have been used. The operating principle of this type of thermometers is based on the temperature dependence of an installed electric resistance. Pt100 thermometers feature a nominal resistance of 100Ω at $0^\circ C$.

Additionally a thermocouple is used by the CTA system. This type of thermometer is based on the Seebeck effect which says that the current flow in a closed circuit consisting of two different metallic conductors is proportional to the temperature of the connection point (see [13, p.129ff]).

3.3 Rotational Speed Sensor

To measure the rotational speed an inductive OMRON E2B proximity sensor has been used. This sensor type consists of a coil that is wound around a ferrite core at the sensor head. A high frequency is applied to this. The generated oscillating electromagnetic field is monitored by an internal circuitry. When a metallic object is moved towards the sensor the mentioned oscillations decrease till they finally stop. When this happens the sensor's output is switched to on. Thus, every passing of a special treated mark rotating with the shaft indicates that another revolution is completed. When simultaneously measuring the time the rotational speed can be determined.

3.4 Flow Rate Measurement

The flow rate is measured with an orifice, one of the Pt100 sensors (see section 3.2) and two Honeywell pressure transducers described in section 3.5.1 which give the static pressure upstream and downstream of the orifice. Their position is qualitatively shown in Fig. 4.1. The calculation to determine the actual mean flow rate is done according to DIN EN ISO 5167 (2013).

Unfortunately the orifice caused a heavily turbulent flow at the inlet. This lead to complications with the time resolved measurements which made a removal of the orifice necessary. To determine the operational point for these measurements the data from the CTA and the ENDEVCO sensor have been used. The flow rate calculation for this case is described in section 5.2.

3.5 Pressure Transducer

3.5.1 Low Time Resolution

For the slow pressure measurements Honeywell 142PC01D pressure transducers have been used. They feature a differential measuring range of $0 \div 6900 \text{ Pa}$ which is satisfactory for the given task. An excitation voltage of 8V is needed.

3.5.2 High Time Resolution

For the time-resolved pressure measurements an piezoresistive ENDEVCO 8506B-2 pressure transducer has been used. Its differential measuring range is 2 psi which equals 13790 Pa . The excitation voltage needed is 10 V and the sensor's sensitivity is 181.0 mV/psi or 0.0263 mV/Pa . The device's time resolution is restricted to 10 kHz by the data acquisition system in the given test stand (see section 3.6). For the purpose of identifying pressure fluctuations due to surge it is still highly satisfactory.

Unfortunately a parasitic frequency equal to the grid frequency could not be suppressed by any of the available power supply units as illustrated in Fig. 3.4. The device resulting in the lowest amplitude at 50 Hz (MANSON EP-613) has been used. Furthermore this oscillation has been filtered away in the data reduction process (see section 5.1.3).

The offset at zero pressure difference has turned out to be 0.8865 mV respectively 33.71 Pa . Hence, the used linear calibration curve was $p = -33.71 \text{ Pa} + 3802.28 \frac{\text{Pa}}{\text{V}} \cdot E$ where E stands for the transducer's output voltage.

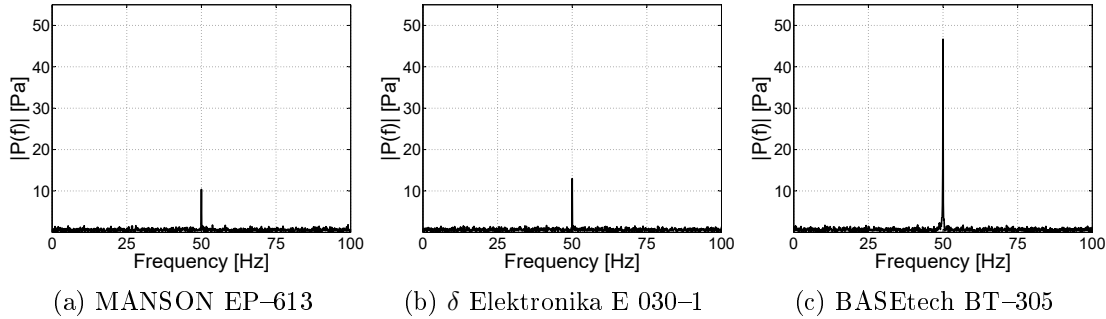


Figure 3.4: Pressure signal spectra at ambient pressure using different power supplies; definition of Fourier transform see below.

3.6 Data Acquisition System

For the data acquisition of the pressure and temperature measurements two USB-6008 by National Instruments have been used. Their maximum sampling rate is 10 kHz .

The CTA uses its own integrated Data acquisition system by DANTEC which is called StreamLine.

Chapter 4

Test Stand Configuration

4.1 General Notes

A scheme of the test stand configuration is given in Fig. 4.1. Additionally some photographs are presented in Appendix B. Due to the limited financial and spatial possibilities at the institute it was not possible to place the throttle downstream of the compressor which would have provided an undisturbed inlet flow. It was also not possible to realize a finite plenum (fixed or adjustable) to study its influence on the system behaviour. Thus, the blower works at free discharge and with an inlet duct as described in DIN EN ISO 5801 (2008), section 26.3. The inlet ducting features a inner diameter of 355 mm .

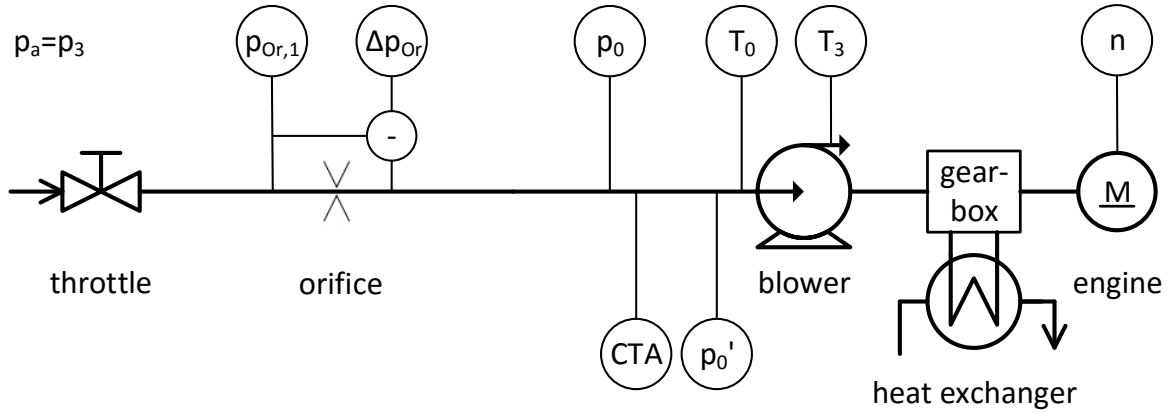


Figure 4.1: Scheme of the test stand configuration.

4.2 Power Converter

The power converter used is a BBC Veritron ASD 6601 which offers a quite accurate current indication with just a minor tendency towards too little values. Its credibility is supported by parallel measurements at the engine itself which have been performed for some selected settings. The results can be seen in Fig. 4.2. The engine's rotational speed is also displayed which allows to determine the corresponding impeller speed additionally to the inductive sensor.

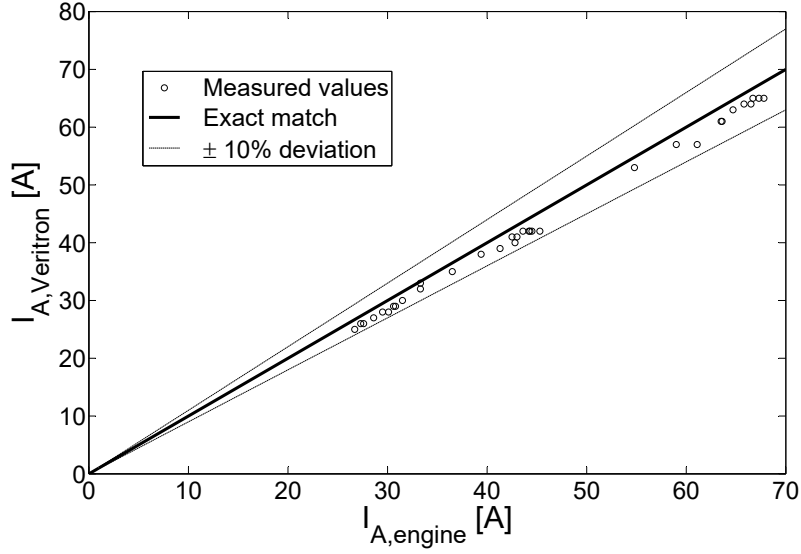


Figure 4.2: Current indication of the power converter compared to the current measured directly at the engine

4.3 Direct Current Motor

The blower is driven by an ELIN G 20 separately excited direct current engine via a gearbox (see section 4.4). This engine has the following specifications.

Voltage:	440 V
Current:	87 A
Power:	34 kW

Electrical excitation for 3000 rpm idle speed:

Exciting voltage:	190 V
Exciting current:	0.26 A

Electrical excitation for 2000 rpm idle speed:

Exciting voltage:	440 V
Exciting current:	0.6 A

4.4 Gearbox

Engine and blower are connected via a single-stage gearbox manufactured by SGP (Simmering-Graz-Pauker) that is featuring an internal gear pump (see below). The transmission ratio between engine and blower is 37/126 respectively 1/3.405. A closer look on the gearbox is presented in [15, p. 13].

4.5 Lubrication and Cooling System

4.5.1 Tothing Oil Supply

The tothing oil supply is ensured by an internal gear pump which is driven by the main train with a transmission ratio of 4/1 respectively 1/0.25.

4.5.2 Bearing Oil Supply

The bearing oil supply is done by an external gear pump which is driven by an AEG MFW 178 rotary current asynchronous engine with a power of 1.8 kW and a rotational speed of 1350 rpm.

4.5.3 Oil Cooling

Both oil pumps are using the same oil reservoir. The warmed oil is being cooled by an oil/water heat exchanger in order to keep the bearing temperatures within a certain band. The water flow rate can be adjusted by hand.

4.6 Blower

4.6.1 General Characteristics

The SGP (Simmering–Graz–Pauker) HR 40/40 is a low pressure ratio centrifugal compressor, with a vaneless diffuser and a spiral housing. Compressors of this class are usually called blowers. The compressor map is known from previous measurements at the institute (see [15]). Its relevant region is presented in Fig. 4.3. For this blower the static and total pressure rise are practically equivalent since D_0 almost equals D_3 and the density can be assumed as constant due to the low pressure difference. This allows to simplify the Gibbs fundamental equation to

$$\Delta h_s = \frac{\Delta p}{\rho}. \quad (4.1)$$

Consequently the isentropic blade loading which is defined as

$$\psi_s = \frac{\Delta h_{s,t}}{\frac{1}{2}u_2^2} \quad (4.2)$$

can also be expressed by

$$\psi_s \approx \frac{\Delta p_t}{\frac{1}{2}\rho u_2^2}. \quad (4.3)$$

A characteristic value commonly used with high performance compressors where compressible effects are important is the pressure ratio

$$\Pi_t = \frac{p_{3t}}{p_{0t}}. \quad (4.4)$$

The flow coefficient φ for radial machines is usually defined as

$$\varphi = \frac{c_{m2}}{u_2}. \quad (4.5)$$

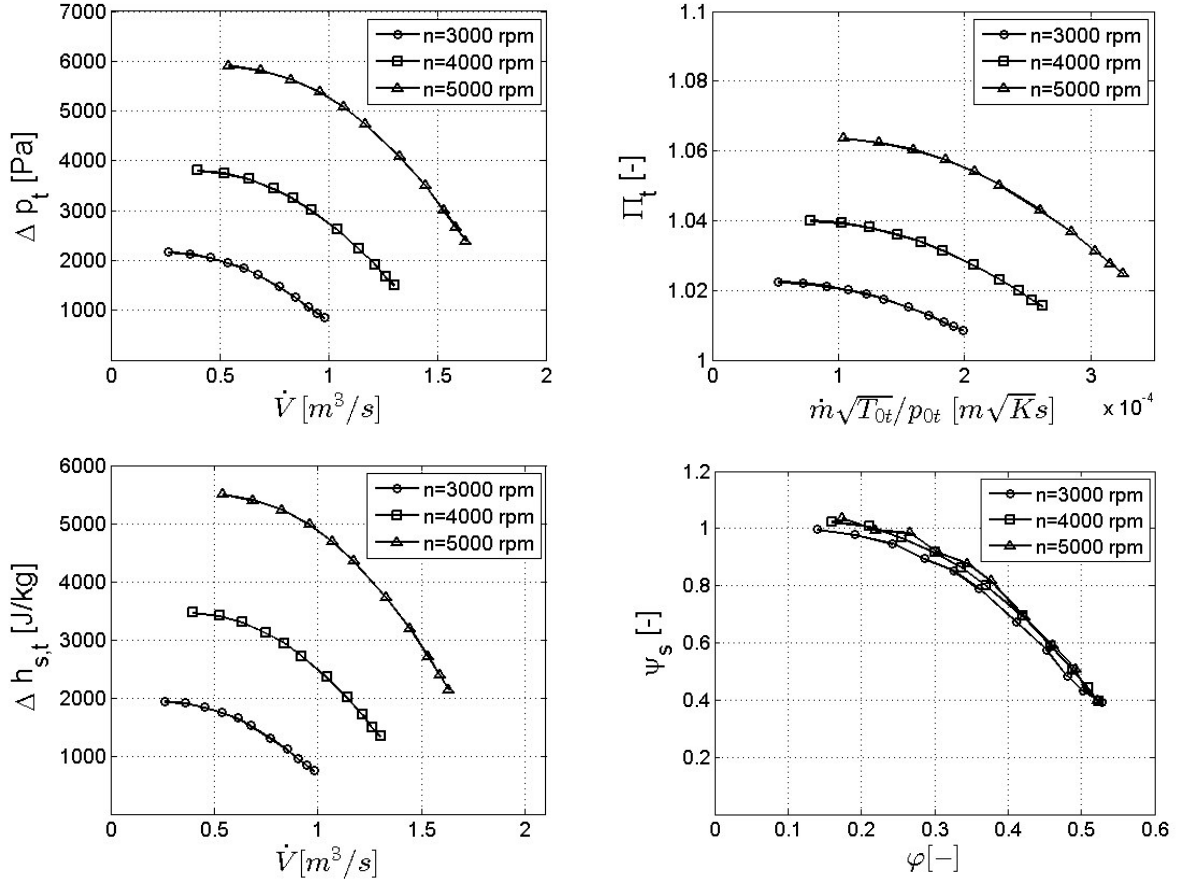


Figure 4.3: Different ways of presenting the SGP HR 40/40 compressor map for the studied speeds.

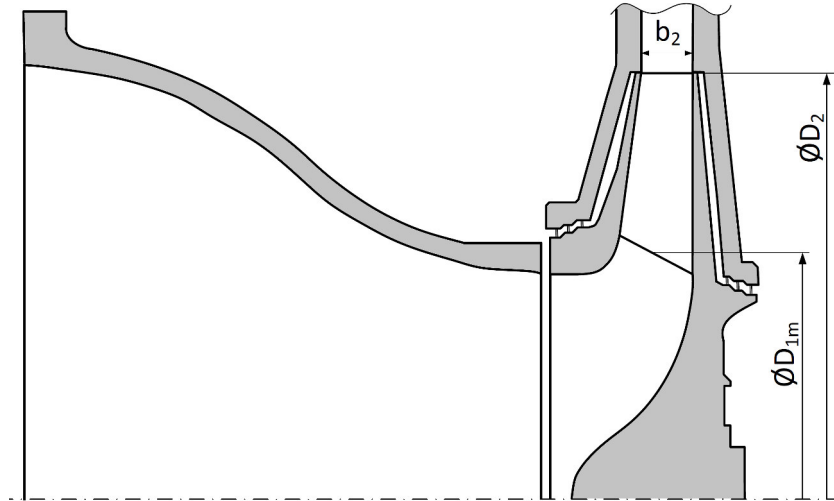


Figure 4.4: Impeller and inlet section of the SGP HR 40/40.

4.6.2 Impeller

The shrouded radial impeller with the dimensions in Tab. 4.1 carries 16 backward curved blades that are mounted with rivets. Its position in the Cordier diagram can be found in Fig. 4.5. The definitions for the dimensionless speed number and diameter number are given by

$$\sigma = \frac{2^{1/4} n \sqrt{\dot{V}} \pi}{\Delta h_s^{3/4}}, \quad (4.6)$$

$$\delta = \frac{D_2 \sqrt{\pi} (\Delta h_s)^{1/4}}{2^{3/4} \sqrt{\dot{V}}}. \quad (4.7)$$

Since it is a wide spread error that the Cordier line represents best efficiency configurations it is worth to mention that in fact classical axial and radial compressors are located on this famous line just because of kinematic reasons as described in [18]. The front and back end are each equipped with three step labyrinth seals.

Mean inlet blade diameter	D_{1m}	230 mm
Outlet blade diameter	D_2	400 mm
Outlet blade height	b_2	24 mm
Inlet complementary relative metal angle	$\beta_{1,m}^+$	37°
Outlet complementary relative metal angle	$\beta_{2,m}^+$	$42^\circ 20'$

Table 4.1: Main dimensions of the SGP HR 40/40 impeller.

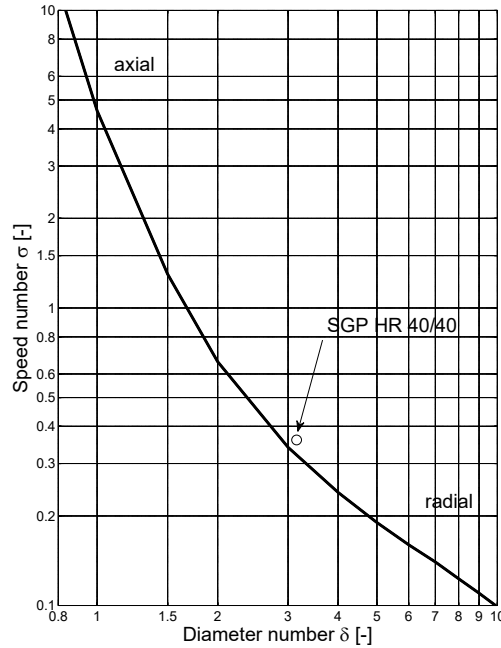


Figure 4.5: The SGP HR 40/40 in the Cordier Diagram; Data taken from [1, p. 79ff].

4.6.3 Diffuser and Volute Housing

As usual with machines of this type the blower is equipped with a vaneless diffuser and a so called volute or spiral housing. Its cross sectional area is increasing almost linearly with the angle as presented in Fig. 4.6. A final linear diameter increase from 286 mm at $\varphi = 360^\circ$ to 350 mm is realized via a straight diffuser.

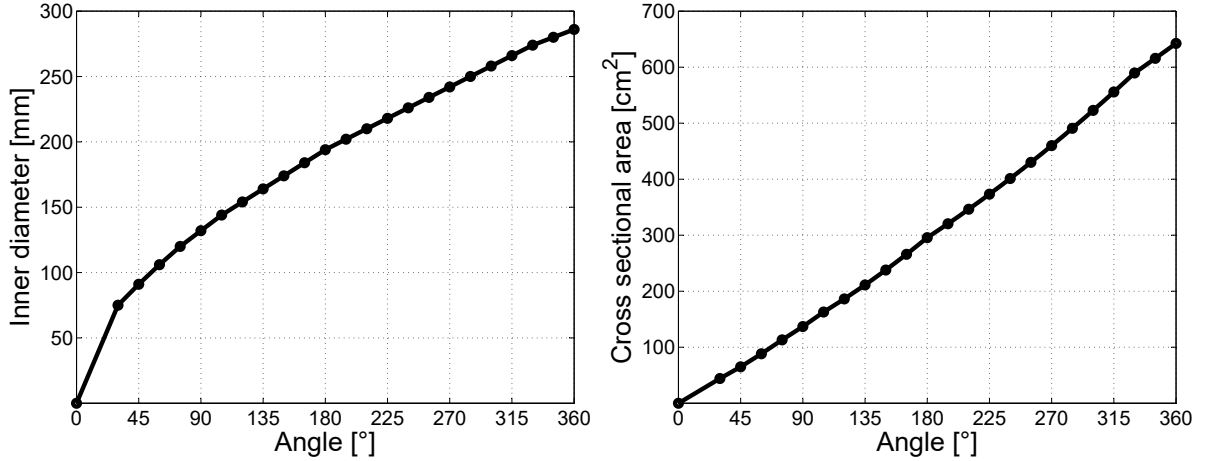


Figure 4.6: Inner diameter and cross sectional area functions of the spiral housing according to design drawings.

4.7 Orifice

The orifice used was carried out according to the specifications in Fig. 4.7 with $\varnothing D_{Or} = 211\text{ mm}$. Since it caused a high turbulence flow it has been removed for most of the transient measurements.

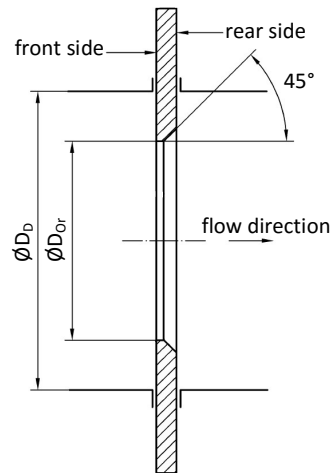


Figure 4.7: Orifice dimensions according to DIN EN ISO 5167 – 2 (2013).

4.8 Throttle

The used throttle was manufactured by Emile Egger & Co. It allows infinitive variable manual adjusting of the effective flow diameter from 0% to 100%. In the fully opened position the clear span of the throttle is $220mm$ which corresponds to an area of $0.0314m^2$. Its closing mechanism is similar to a camera diaphragm (see also the photographs in Appendix B).

4.9 Computers

Two computers have been used at the described test stand. A rather old one for the CTA measurements since the integration of this equipment to a more modern system is fairly complicated, and another for all other measurements. Their arrangement can be seen on photographs in Appendix B with the computer used for CTA on the left.

Chapter 5

Data Analysis

5.1 Time-Series Analysis

5.1.1 Fourier Transform, Discrete Fourier Transform (DFT) and Fast Fourier Transform (FFT)

In order to be able to find dominant frequencies in a signal – as here to identify surge – it is desirable to obtain the signal's amplitude as a function of the corresponding frequency. Therefore, the so called (continuous) Fourier transform is used which is defined as

$$X(f) = \int_{-\infty}^{\infty} x e^{-j2\pi ft} dt. \quad (5.1)$$

Usually one is confronted with a finite number of discrete values when performing experimental measurements. Thus, one has to do a DFT which gives a discrete spectrum. This transform is achieved by

$$X(f_k) = \frac{1}{N} \sum_{n=0}^{N-1} x_n e^{-j2\pi nk/N}, \quad n, k = 0, \dots, N-1. \quad (5.2)$$

The DFT takes $\mathcal{O}(N^2)$ arithmetical operations which means a rapidly increasing need for computing capacity when increasing the number of points. Fortunately it is possible to improve the transform's performance by using a FFT algorithm which is factorizing the DFT matrix into a product of sparse factors. Then just $\mathcal{O}(N \log N)$ operations are needed. This algorithm's speed is best when using a signal length that is a power of two.

Since the time-history record $y(t)$ of a finite time T is extended to an unlimited periodic time-history record one is confronted with so called spectral leakage (except the signal is in fact T-periodic). This means that the computed spectrum contains frequencies that do not occur in the analysed (infinite) signal. In order to suppress this effect window functions are used which are fading out the signal at the ends of the interval. Commonly used window functions together with their corresponding spectra are presented in Fig. 5.1.

When it comes to select an appropriate window function the main criteria correspond to their spectral shape. Two important ones are the bandwidth of the main lobe and the peak level of the side lobes. For the thesis at hand the Hamming window was used which is defined as

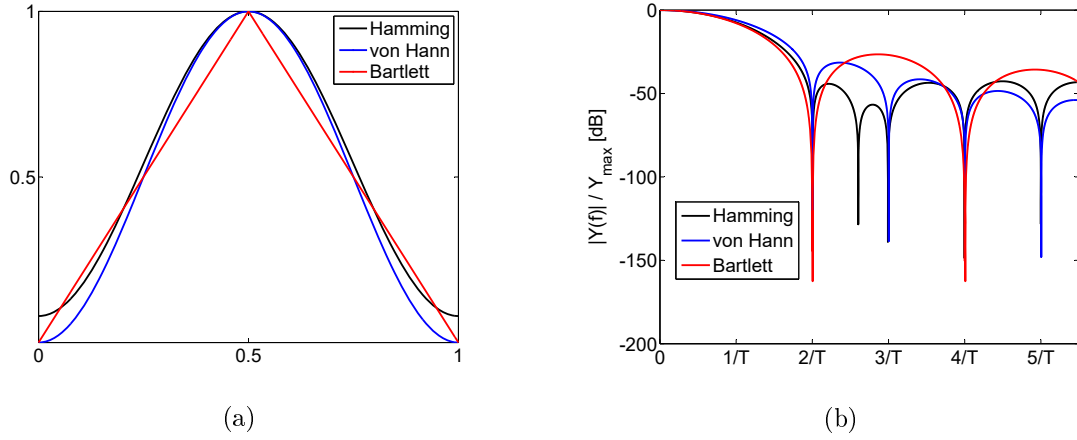


Figure 5.1: Commonly used window functions (a) and their corresponding spectra (b).

$$f_{\text{Hamming}}(n) = 0.54 - 0.46 \cos\left(2\pi \frac{n}{N}\right), \quad 0 \leq n \leq N. \quad (5.3)$$

In general the use of any of these tapering operations to minimize the side lobe leakage will result in a broader bandwidth of the main lobe and consequently a lower frequency selectivity. This can be countered by increasing the block duration T and by overlapping the blocks. For the analysis within this work an overlapping of 50% has been chosen.

5.1.2 Auto and Cross Correlation

As described for example in [3, p. 428ff], the autocorrelation function allows to obtain an assessment of the general dependence of time-history record values at one time on values at another time. It allows to detect periodic components of the signal and is used to calculate the integral time-scale and integral length-scale which are characteristic values for a turbulent flow. The autocorrelation between two values at different times can be formulated as

$$r_{xx}(\tau) = \lim_{T \rightarrow \infty} \frac{1}{T} \int_0^T x(t) x(t + \tau) dt. \quad (5.4)$$

To study the general dependence between two different sets of values, e. g. pressure and velocity measurement results, the crosscorrelation function is used. If the signals have components in common it is possible to determine a characteristic time delay. The crosscorrelation function is defined in a similar manner as the autocorrelation function as

$$r_{xy}(\tau) = \lim_{T \rightarrow \infty} \frac{1}{T} \int_0^T x(t) y(t + \tau) dt. \quad (5.5)$$

5.1.3 Filtering

IIR Notch Filter

As mentioned in section 3.5.2 the ENDEVCO pressure signal exhibits a dominant parasitic frequency at 50 Hz . To eliminate this peak in the spectrum a second order IIR (Infinite Impulse Response) notch filter has been used. The necessary inputs are the normalized frequency at which the notch shall be located and the bandwidth at -3 dB amplification. Therefore, the frequency is normalized by the Nyquist frequency. This frequency is half the sampling frequency and the highest frequency that can be detected for a given sampling rate.

Low Pass Filter

For some studies it was advantageous to filter frequencies that are too high to be related to surge. Therefore, a first order Butterworth low pass filter has been used. Apart from order and filter type the only necessary input is the normalized cutoff frequency.

5.1.4 Turbulence Intensity

The first step in describing turbulence in a measured flow is to separate the velocity's mean value from its fluctuating part. This can be done in all spatial directions. Thus, we define

$$u = \bar{u} + u', \quad v = \bar{v} + v', \quad w = \bar{w} + w', \quad (5.6)$$

where u , v and w stand for the spatial velocity components in this context. During the data analysis the mean value is found by arithmetic averaging. Now the most basic quantity to describe a turbulent flow, the turbulence intensity, can generally be defined as

$$Tu = \sqrt{\frac{\frac{1}{3} (\overline{u'^2} + \overline{v'^2} + \overline{w'^2})}{\overline{u^2} + \overline{v^2} + \overline{w^2}}}. \quad (5.7)$$

For isotropic turbulence which is assumed for the given test stand configuration the relations

$$\overline{u'^2} = \overline{v'^2} = \overline{w'^2} \quad (5.8)$$

are valid which allow to simplify Eq. (5.7) to

$$Tu = \frac{\sqrt{\overline{u'^2}}}{\bar{u}}, \quad (5.9)$$

which can be determined using a single-wire probe. Switching back to the usual nomenclature within this work one can now write

$$Tu = \frac{\sqrt{\overline{c'^2}}}{\bar{c}}. \quad (5.10)$$

5.2 Compressor Map Measurement

For the compressor map measurement two different approaches have been applied. The classic one has been carried out according to DIN EN ISO 5167 (2013). For this method several iterations and the repeated solution of an equation system was necessary. The Matlab code used is given in Appendix A.

For the compressor map measurement based on the hot-wire probe and the fast response pressure probe a simple assumption on the turbulent velocity profile had to be made. Therefore, the power law

$$\bar{c}(r) = \bar{c}_{max} \left(1 - \frac{r}{R}\right)^{\frac{1}{m}} \quad (5.11)$$

has been applied (see [16, p. 198ff]). The mean value is consequently given by

$$\bar{c}_m = \frac{1}{R^2 \pi} \int_0^{2\pi} \int_0^R \bar{c}(r) r dr d\varphi \quad (5.12)$$

$$= \frac{2 \bar{c}_{max}}{R^2} \int_0^R r \left(1 - \frac{r}{R}\right)^{\frac{1}{m}} dr \quad (5.13)$$

$$= \frac{2 \bar{c}_{max} m^2}{2m^2 + 3m + 1}. \quad (5.14)$$

The exponent m has been interpolated depending on the Reynolds number (see Tab. 5.1). Because of that iterations were necessary. The code is given in Appendix A.

Re	$4 \cdot 10^3$	10^5	$6 \cdot 10^5$	$1.2 \cdot 10^6$	$2 \cdot 10^6$
m	6	7	8	9	10

Table 5.1: Exponent m for different Reynolds numbers according to [16, p. 201].

5.3 Inlet Flow Angle

An interesting value for the onset of instability is the deviation of the inlet incidence angle. With the definitions in Fig. 5.2 and assuming $\alpha_1 = 90^\circ$ it follows from

$$\beta_1^+ = \arctan \frac{c_1}{u_1}. \quad (5.15)$$

The absolute velocity c_1 is known from the CTA measurement and the mean circumferential velocity at the blade inlet u_1 is known from the rotational speed and the impeller radius. Again assuming $\alpha_1 = 90^\circ$ the relative velocity value can be calculated by

$$w_1 = \sqrt{c_1^2 + u_1^2}. \quad (5.16)$$

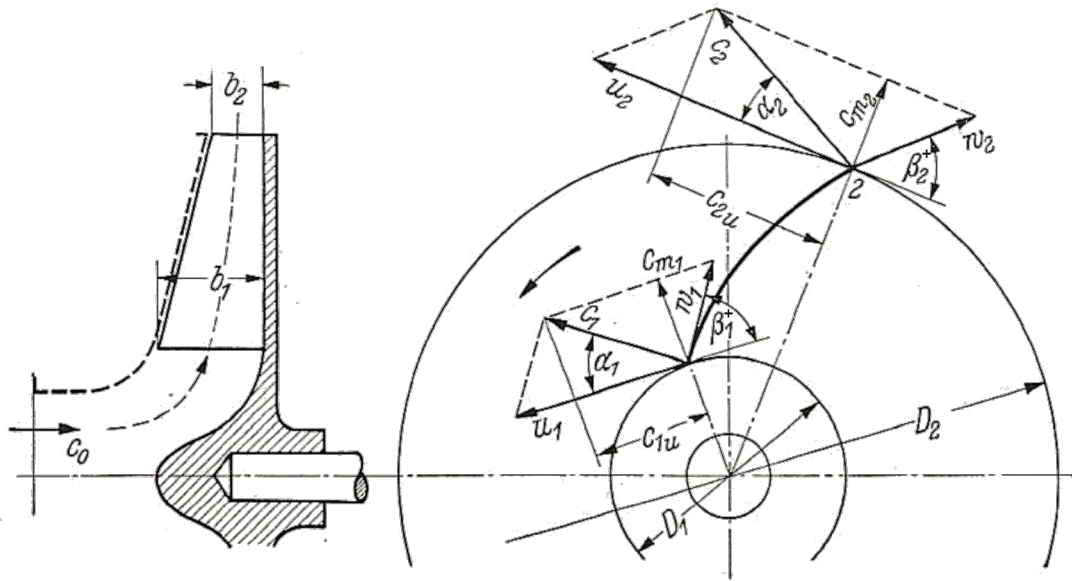


Figure 5.2: Velocity triangles respectively parallelograms of a centrifugal compressor stage; taken from [6, p.329] and adapted.

Chapter 6

Measurement Results

6.1 Compressor Map

As a first step the classical method to obtain the compressor map using the orifice flow rate measurement and slow temperature and pressure sensors has been performed. The results which are in accordance with the results presented in [15] have already been presented in Fig. 4.3.

Since the orifice had to be removed for the main part of this study this method could not be used to determine the surge line. Thus, the mean values of the fast sensors had to be used. For the flow rate measuring the velocity profile described in section 5.2 has been assumed. A comparison of the maps obtained with both mentioned methods is given in Fig. 6.1. The deviation is caused by the uncertainty of the velocity profile assumption and by the comparably high uncertainty of the fast sensors concerning the measured mean values. This is especially the case with the pressure transducer due to its age and the little documentation available.

For the dimensioned calculations in section 2.3.3 a 7th order polynomial fit defined by

$$\Delta p_s = C_1 \dot{m}^7 + C_2 \dot{m}^6 + \dots + C_7 \dot{m} + C_8 \quad (6.1)$$

has been created. The form as a function of mass flow rate was defined to be appropriate to the analytical approach. To achieve an information about mass flow rate a density of $\rho = 1.189 \text{ kg/m}^3$ has been assumed. The polynomial's coefficients are given in Tab. 6.1. The order of this fit has been chosen since lower order approximations were not able to represent the very left part of the characteristics sufficiently well and higher order approximations exhibited oscillatory behaviour within the measured part of the characteristics. Hence, the chosen function appears to be a good compromise as illustrated in Fig. 6.2.

For the dimensionless analysis a 5th-order polynomial fit of the left part of the characteristic defined by

$$\Delta \tilde{p}_s = C_1 \dot{\tilde{m}}^5 + C_2 \dot{\tilde{m}}^4 + \dots + C_5 \dot{\tilde{m}} + C_6 \quad (6.2)$$

has been created. Additionally to the measured points two estimated points at lower mass flows have been added to obtain a negatively sloped branch of the characteristic close to zero mass flow. The coefficients of this fit are given in Tab. 6.2. The order of the fit was again a compromise between accuracy and oscillatory behaviour.

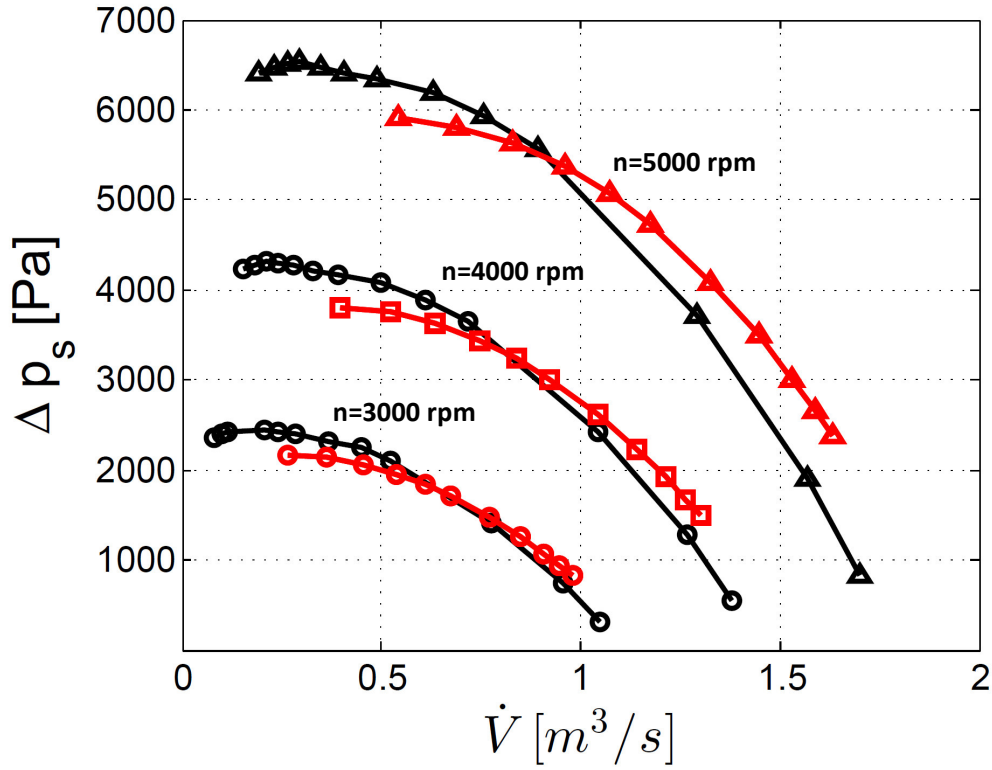


Figure 6.1: Comparison of measured compressor map, orifice (red) and fast sensor (black) measurements.

Coefficients	$\Delta p_s(\dot{V})$ for 3000 rpm [Pa s/m ³] · 10 ⁵	$\Delta p_s(\dot{V})$ for 4000 rpm [Pa s/m ³] · 10 ⁵	$\Delta p_s(\dot{V})$ for 5000 rpm [Pa s/m ³] · 10 ⁵
C_1	$0.9855 \text{ Pa s}^7/\text{m}^21$	$0.4317 \text{ Pa s}^7/\text{m}^21$	$0.1305 \text{ Pa s}^7/\text{m}^21$
C_2	$-4.1816 \text{ Pa s}^6/\text{m}^18$	$-2.4290 \text{ Pa s}^6/\text{m}^18$	$-0.8969 \text{ Pa s}^6/\text{m}^18$
C_3	$7.1556 \text{ Pa s}^5/\text{m}^15$	$5.5385 \text{ Pa s}^5/\text{m}^15$	$2.5016 \text{ Pa s}^5/\text{m}^15$
C_4	$-6.3277 \text{ Pa s}^4/\text{m}^12$	$-6.5659 \text{ Pa s}^4/\text{m}^12$	$-3.6333 \text{ Pa s}^4/\text{m}^12$
C_5	$3.0816 \text{ Pa s}^3/\text{m}^9$	$4.3137 \text{ Pa s}^3/\text{m}^9$	$2.9291 \text{ Pa s}^3/\text{m}^9$
C_6	$-0.8422 \text{ Pa s}^2/\text{m}^6$	$-1.5740 \text{ Pa s}^2/\text{m}^6$	$-1.3180 \text{ Pa s}^2/\text{m}^6$
C_7	$0.1160 \text{ Pa s}/\text{m}^3$	$0.2883 \text{ Pa s}/\text{m}^3$	$0.2998 \text{ Pa s}/\text{m}^3$
C_8	0.0183 Pa	0.0227 Pa	0.0387 Pa

Table 6.1: Coefficients of the 7th-order polynomial curve fit of the compressor characteristics.

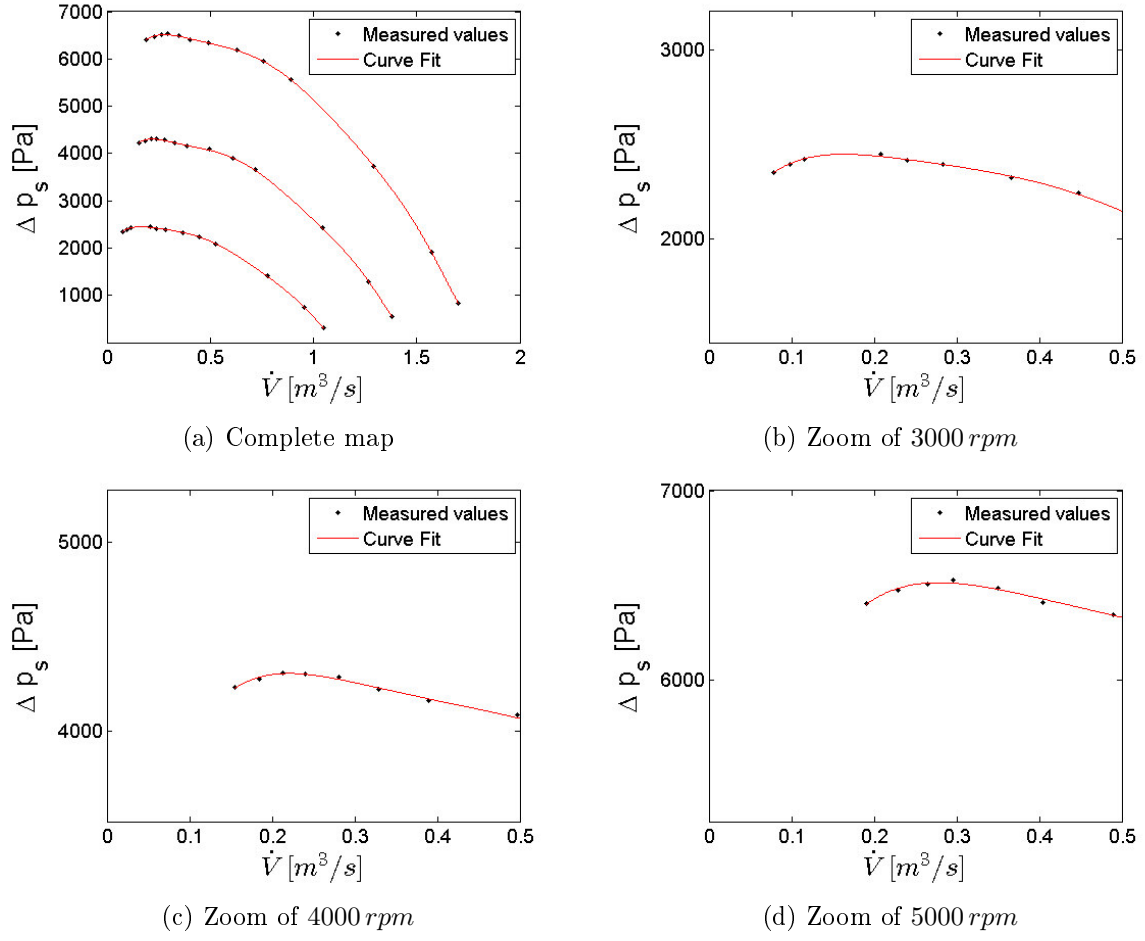


Figure 6.2: Illustration of the polynomial curve fit of the compressor map.

Coefficients	$\Delta \tilde{p}_s(\dot{m}_T)$ for 3000 rpm [-]	$\Delta \tilde{p}_s(\dot{m}_T)$ for 4000 rpm [-]	$\Delta \tilde{p}_s(\dot{m}_T)$ for 5000 rpm [-]
C_1	-2136873.2	-1488053.4	-1873277.3
C_2	466296.9	337634.2	423849.4
C_3	-36159.5	-27321.1	-34283.1
C_4	1135.8	896.8	1138.0
C_5	-11.9	-10.1	-13.1
C_6	1.0	1.0	1.0

 Table 6.2: Coefficients of the 5th-order polynomial curve fit of the left part of the dimensionless compressor characteristics.

6.2 Time Domain Analysis

In order to witness the onset of surge measurements, during closing from the stable to the unstable section of each characteristic have been performed. The results of these measurements can be seen in Fig. 6.3 and Fig. 6.4. While the onset of surge can clearly be seen in the pressure signal there is optically no significant change in the velocity signal – except a continuous decrease of course. Nevertheless, it is not possible to locate the surge line based on this records since no triggering between the pressure and the velocity measurement was applied. This means that no relation between an event in the pressure record and a corresponding flow rate can be made. In other words, the operational point at which the pressure oscillations start can not be determined from these signals.

However, at constant throttling in the unstable area it is possible to establish a relation between the pressure and the velocity signal. Since both should exhibit low frequency oscillations with the same period time it should be possible to find a characteristic time shift applying a cross correlation (see section 5.1.2). To achieve a result that is not distorted by stochastic fluctuations a low pass prefiltering has been applied. If a characteristic time lag can be identified it is possible to match the signals with a shift of a quarter period as described in section 2.2.2. Of course it is necessary for this purpose to know the surge frequency as well (see section 6.3). Unfortunately the time lag corresponding to the maximum of the cross correlation function is greater than a period. This could be caused by slight changes of the surge cycle's course over time. This explanation is also supported by the existence of considerable side lobes (see Fig. 6.5). The respective side lobe within a period time around zero served as a basis for the plotting of the surge cycles in Fig. 6.7 and 6.8. It is clear that these plots should be handled with caution since they are subject to considerable uncertainties.

Additionally, if no characteristic time lag can be found for a certain flow rate this indicates that there is no related low frequency oscillation. Thus, the shape of the cross correlation function can serve as a criterion for the surge line identification as well (see Fig. 6.6).

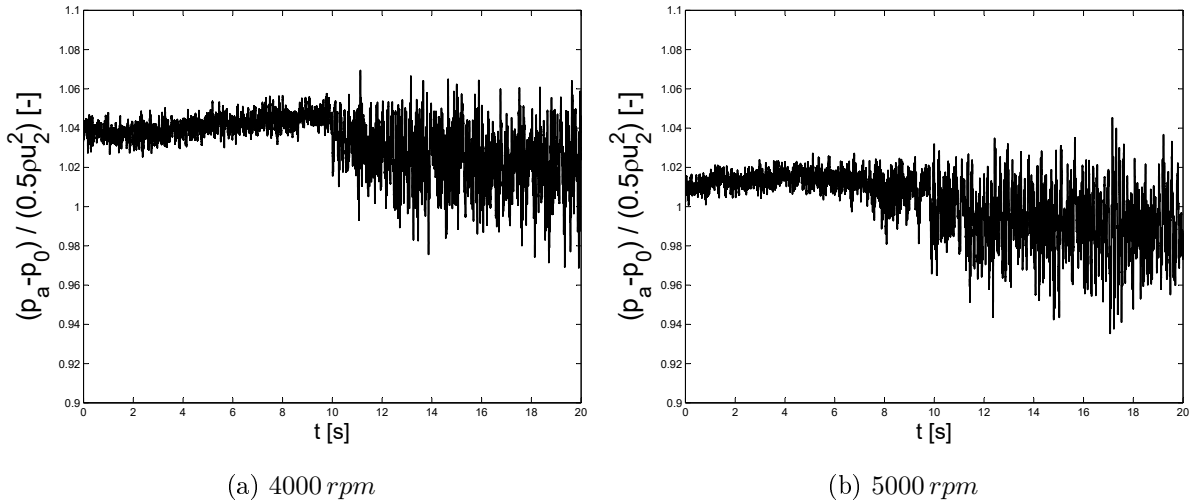


Figure 6.3: Pressure during throttle closing to lowest flow rate.

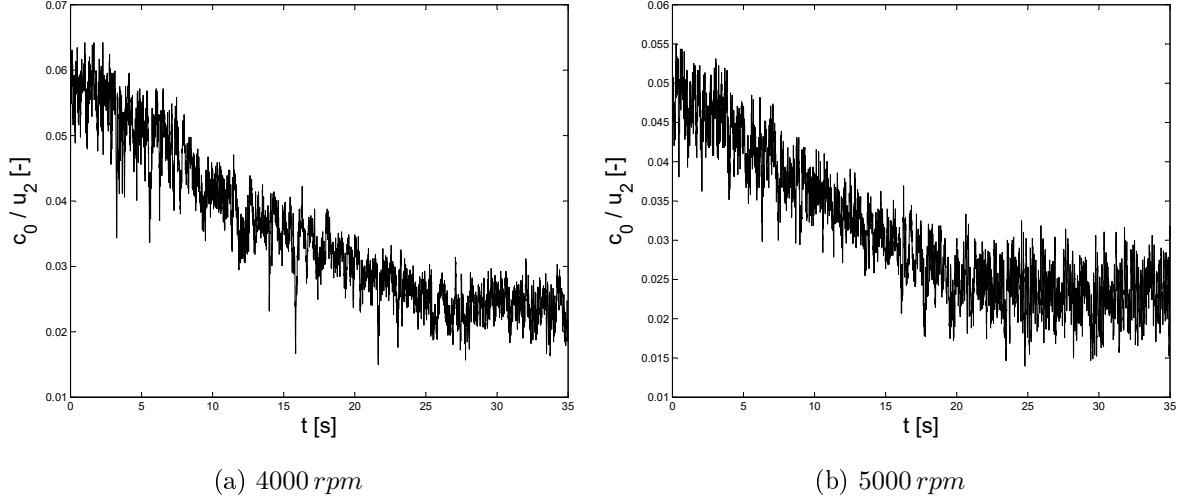


Figure 6.4: Velocity during throttle closing to lowest flow rate.

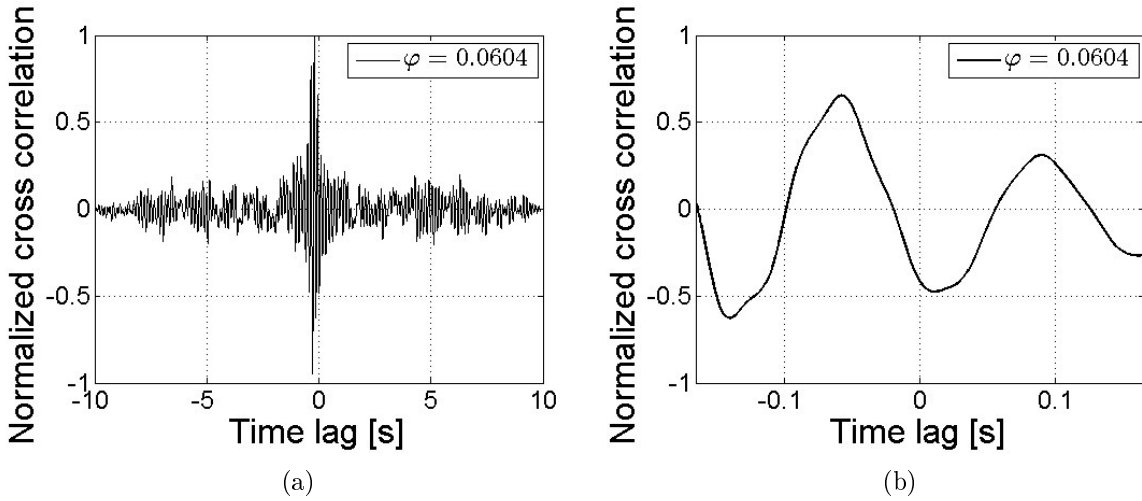


Figure 6.5: Cross correlation between pressure and velocity signal for minimum flow rate at 5000 rpm showing a main lobe at $-0.2064s$ in (a) and a side lobe at $-0.0580s$ in (b).

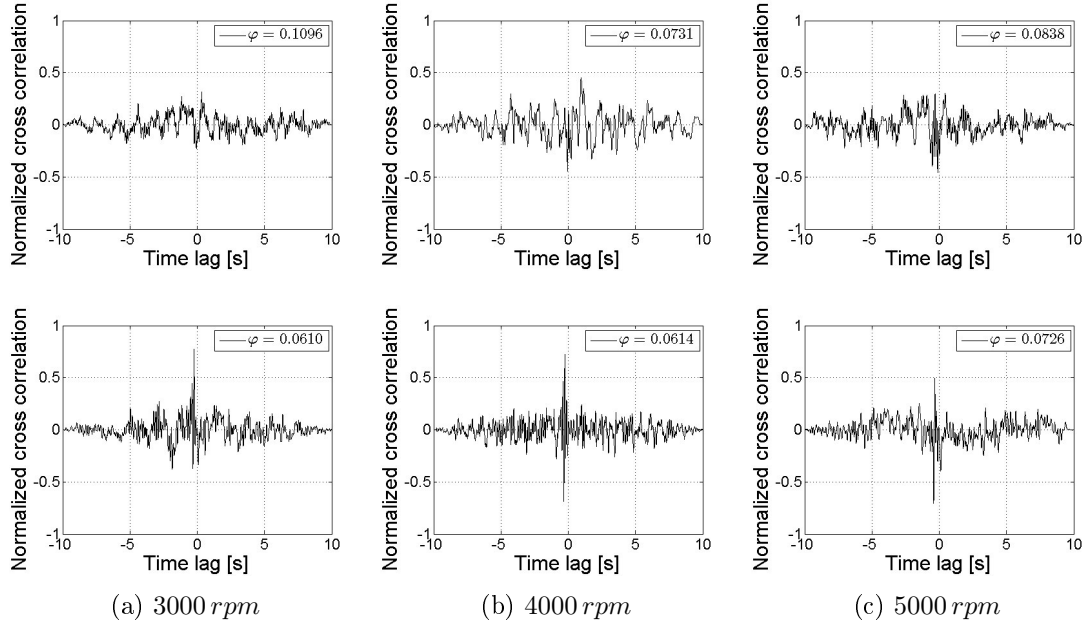


Figure 6.6: Normalized cross correlation functions as a measure for surge inception

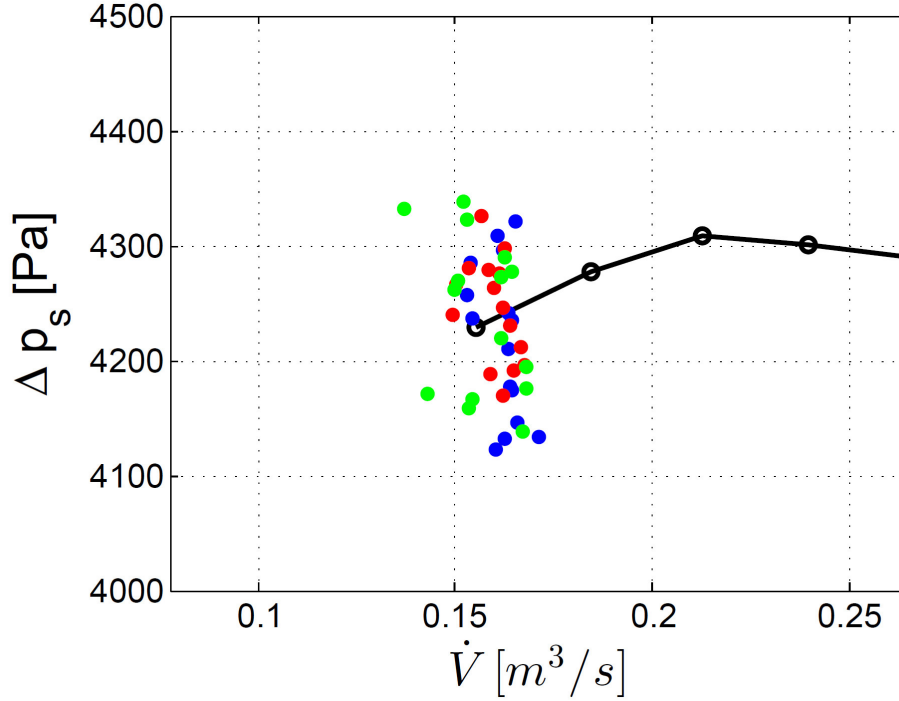


Figure 6.7: Surge cycles with delay of a few seconds for 4000 rpm, each marked with a different color.

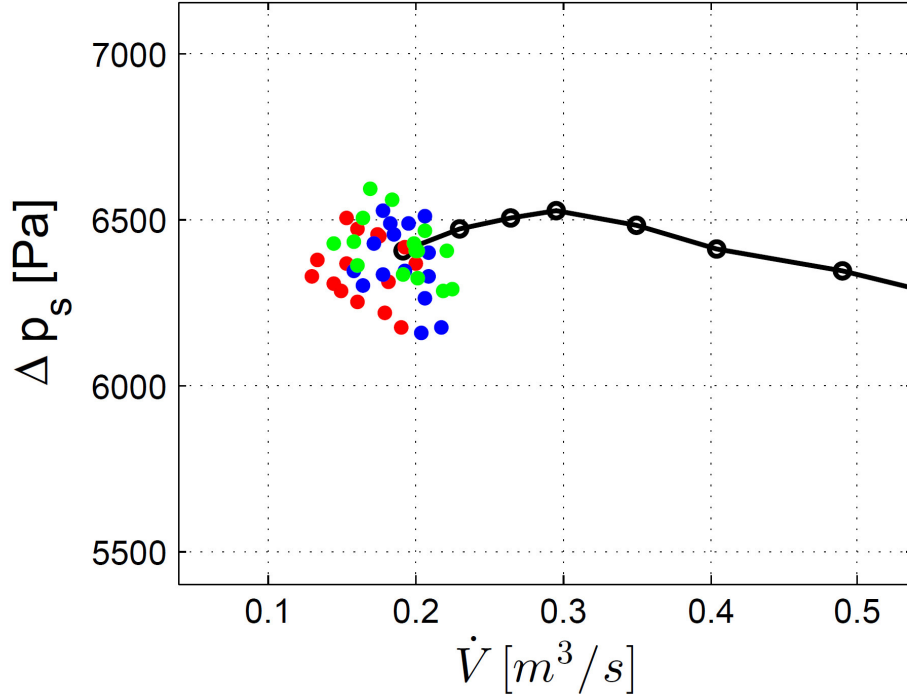


Figure 6.8: Surge cycles with delay of a few seconds for 5000 *rpm*, each marked with a different color.

6.3 Frequency Domain Analysis

A frequency domain analysis of the pressure and the velocity signal can provide information about the two basic questions, when surge occurs, and, at what frequency this oscillatory behaviour takes place.

Figure 6.9 gives an impression of how the velocity spectra change when surge occurs. Although the spectrum in the stable operational range looks fundamentally different from that in a clearly unstable operational point this analysis gives no clear result on the surge line location. Whether the spectrum for $\varphi = 0.08$ and 4000 *rpm* for example already reflects surge or not is a difficult question. Therefore, it is a matter of personal assessment what spectrum corresponds to the onset of instability.

A look at the pressure spectra (see Fig. 6.12) does not improve the situation a lot since the peaks at the surge frequency do not arise suddenly at a specific flow rate. Furthermore, the pressure signals exhibit dominant frequencies which do not occur (to that extent) in the velocity signals. One would probably take no notice of these frequencies in the velocity spectrum if not searching for them. These oscillations are independent of the rotational speed which rules out rotating stall as a source because this phenomenon would lead to dominant frequencies at some fraction of the rotor speed. However, the relevant dominant frequency for surge can just be the lowest one.

Figures 6.10 and 6.11 finally give spectra in the unstable area with the highlighted surge frequencies. Their values are given in Tab. 7.2. For all measurements at a given setting the measuring period was 10 s and the signals have been divided in eight windows with an overlapping

of 50%. This means that each window had a length of 2.22 s which results in a frequency resolution of 0.45 Hz.

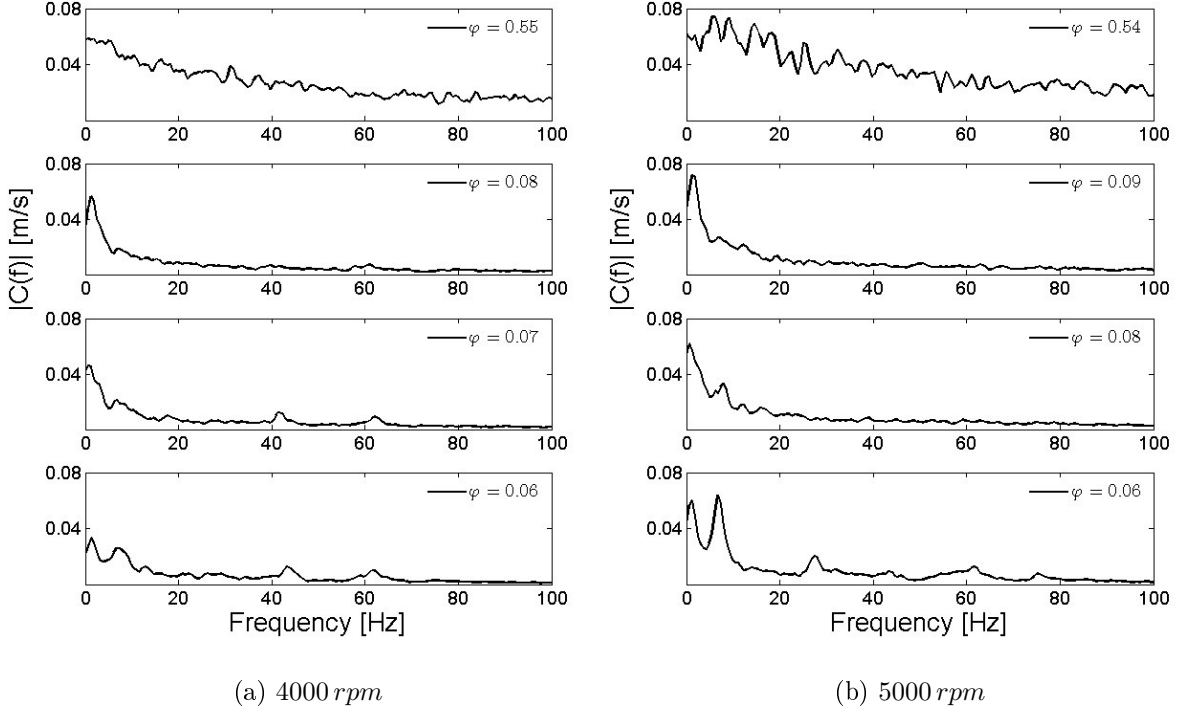


Figure 6.9: Velocity spectra when throttling from highest to lowest flow rate.

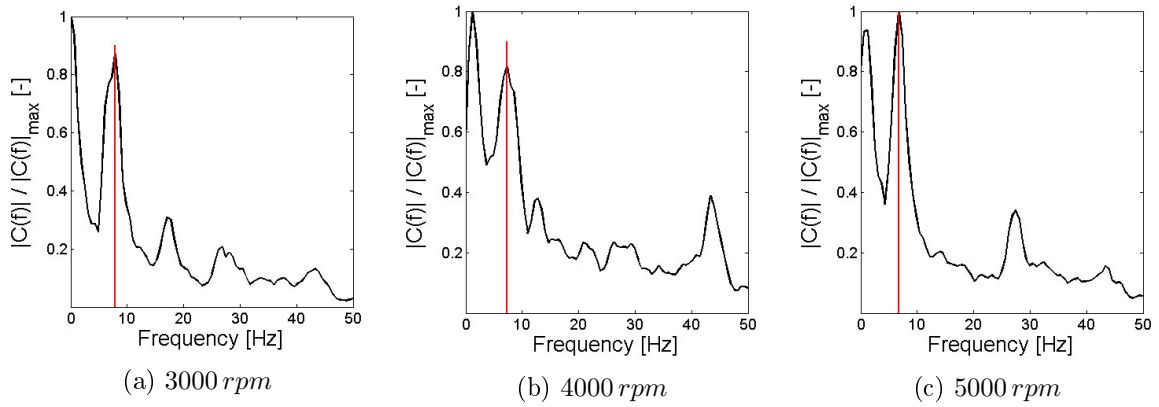


Figure 6.10: Velocity spectra during surge, surge frequencies highlighted.

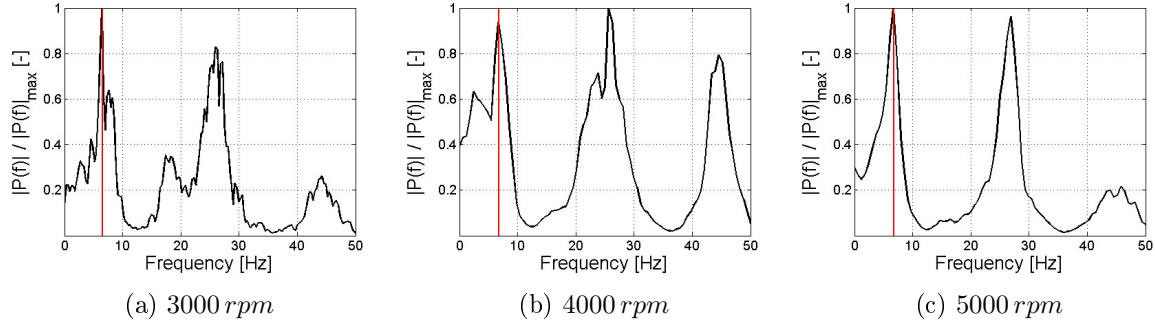


Figure 6.11: Pressure spectra during surge, surge frequencies highlighted.

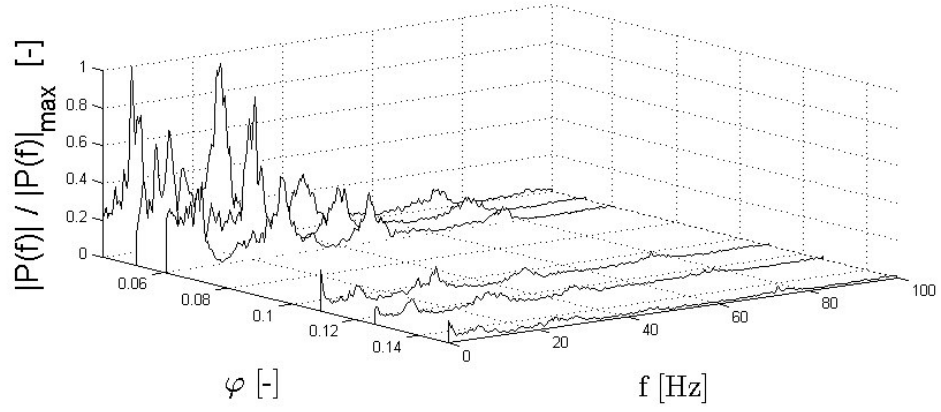
6.4 Inlet Flow Angle

As described in section 5.3 the mean inlet flow angle can be calculated in a one-dimensional way from geometry, rotational speed and flow rate. Carrying out this calculation the results presented in Fig. 6.13 are achieved. In this figure the measured flow rates are marked as well. The values of $\Delta\beta_1^+$ for the critical flow rates are located between -25° and -30° . This corresponds to an actual inlet flow angle β_1^+ of 12° to 7° which results in a quite flat velocity triangle.

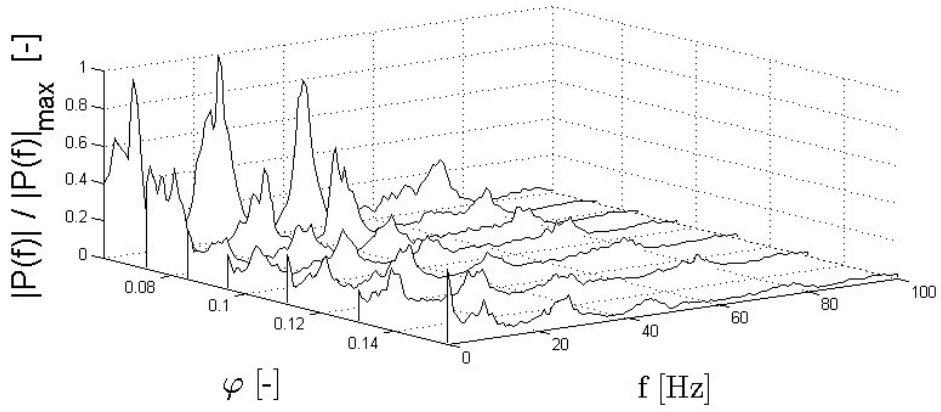
6.5 Turbulence Intensity

The measured turbulence intensity compared to the one predicted according to section 2.4 (see Fig. 6.14) give a qualitatively good agreement whereas their absolute values differ a lot. It has to be emphasized that the RMS-values used for the prediction are the ones of the static compressor measurement. Therefore, it is worth to check their accordance with the RMS-values of the fast pressure measurements. This comparison is illustrated in Fig. 6.15 which shows that for the flow rates studied in the static measurements the accordance seems to be quite good.

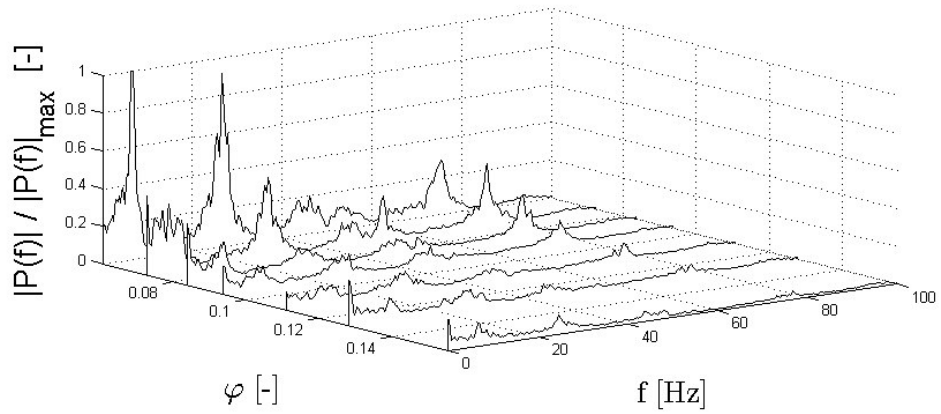
Another question to answer is if the assumption $\frac{1}{2}\rho\overline{c'^2} \approx p_{RMS} = \sqrt{p'^2}$ can be justified. It turns out that this is the main reason for the big quantitative difference of measured and predicted turbulence intensity. Values of p_{RMS} are typically two orders of magnitude greater than values of $\frac{1}{2}\rho\overline{c'^2}$ for this application. Also their qualitative behavior is different as presented in Fig. 6.16. This means that the simple approach in section 2.4 can not be supported by measurements. Nevertheless, Tu and p_{RMS} exhibit a qualitatively similar behaviour.



(a) 3000 rpm



(b) 4000 rpm



(c) 5000 rpm

Figure 6.12: Pressure spectra when throttling to lowest flow rate.

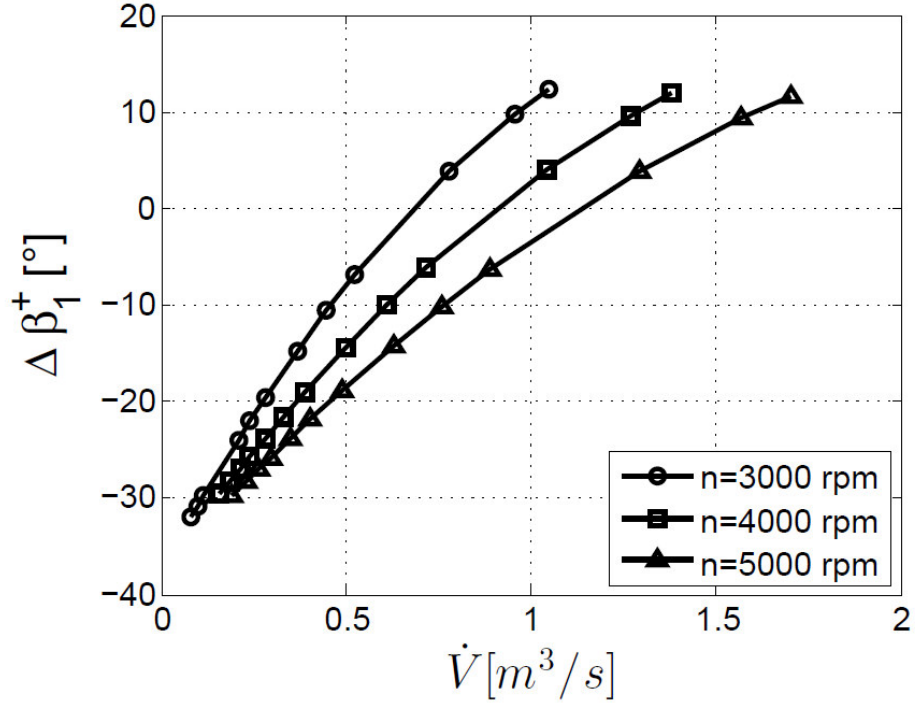


Figure 6.13: Deviation of inlet flow angle from blade angle; markers represent measured flow rates.

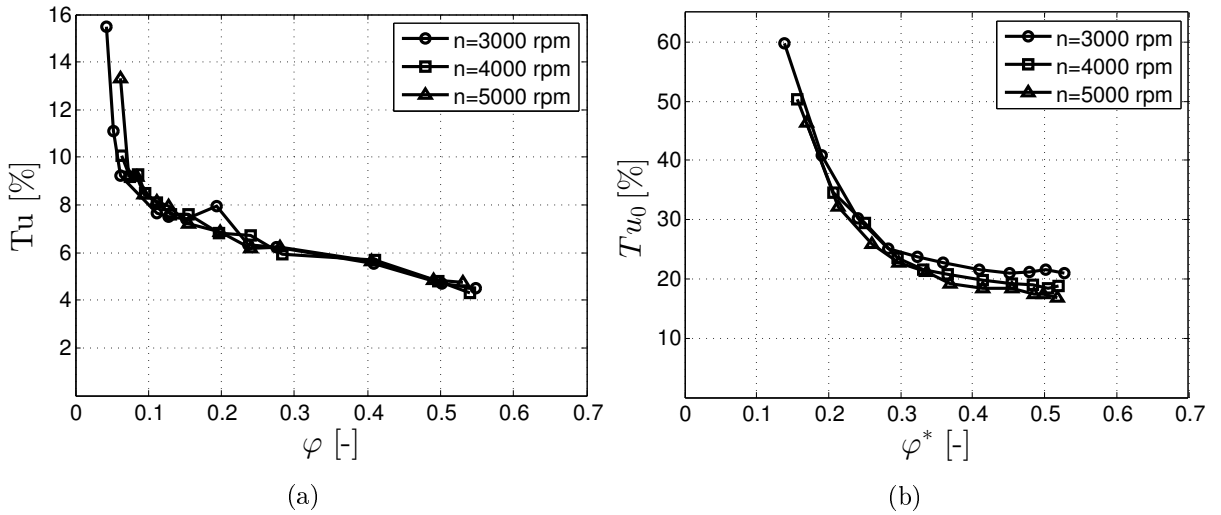


Figure 6.14: Comparison of measured (a) and predicted (b) turbulence intensity.

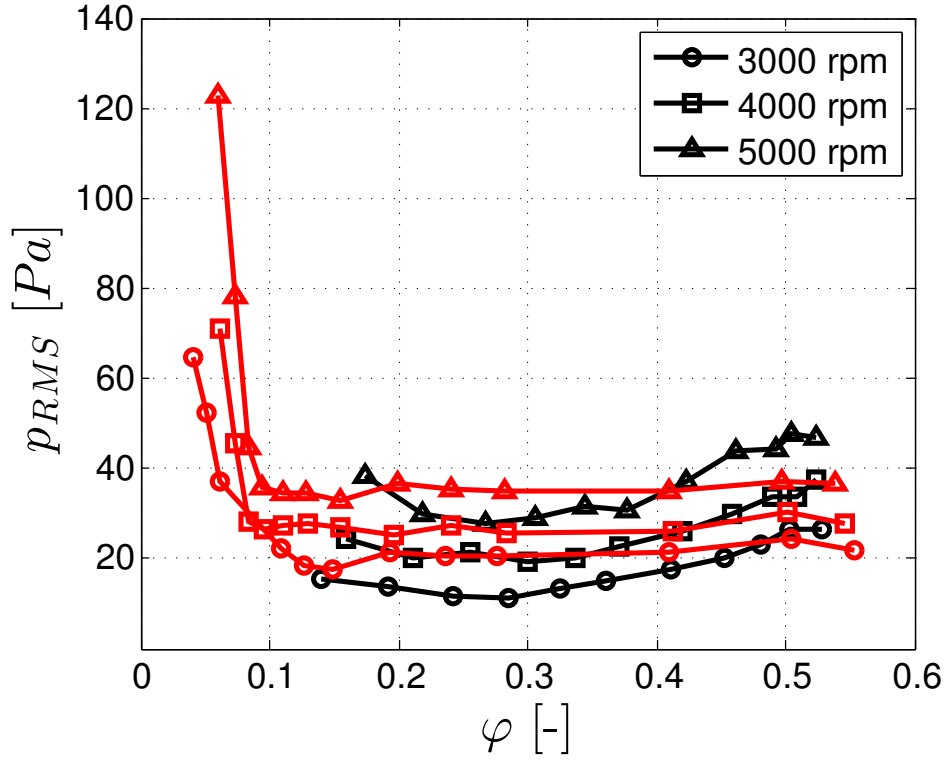


Figure 6.15: Comparison of the RMS-values measured by the slow Honeywell (black) and the fast ENDEVCO (red) pressure transducer.

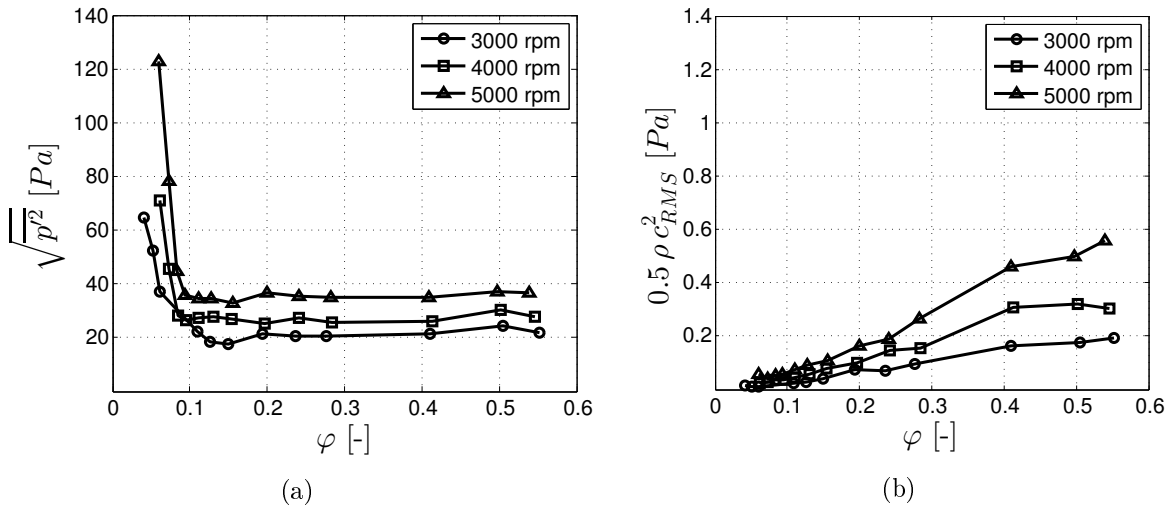


Figure 6.16: Comparison of $\sqrt{p'^2}$ and $0.5 \rho c'^2$.

Chapter 7

Summary and Conclusions

The first approach that has been made within this thesis was an analytical investigation of the overall system behaviour. A detailed simulation of the present test stand has not been possible due to its fixed configuration. Nevertheless, it has been possible to show that the operational point corresponding to the onset of surge must be located on the positively sloped branch of the compressor characteristic. Furthermore, a greater plenum volume lead to a surge limit closer to the maximum pressure rise in this analysis. Now, the plenum volume for the given test stand is practically infinite. Therefore, this analysis suggested that no stable operation on the positively sloped part of the characteristic can be established.

In a second step measurements have been performed in order to verify this prediction. The inlet velocity as well as the inlet pressure have been measured with sensors featuring low and high time resolution. The compressor map measurement based on the integral procedure described in DIN EN ISO 5167 (2013) is more accurate than that based on the fast sensors. Fortunately the agreement was good enough to justify the determination of the surge line using only the high time resolution sensors. This has been necessary since the orifice caused a highly turbulent inlet flow and disturbed the surge detection.

To define the onset of stall two criteria have been applied. The first one deals with the cross correlation between the pressure and the velocity signal. If a characteristic time lag – or in other words a correlation – between these two time records could be found at a given operational point this point has been considered as unstable. The resulting values are presented in Tab. 7.1.

The second criterion is based on the velocity and surge spectra. An unstable operational point is thereby characterized by a corresponding spectrum with a significant peak at a low frequency ($5 \div 10 \text{ Hz}$). Additionally to the location of the surge line this investigation also gives the surge frequency. The results are given in Tab. 7.2. Both results are also graphically presented in Fig. 7.1. It can clearly be seen that the onset of instability is located at the maximum pressure rise or close to it as predicted by the lumped parameter model.

The described investigations provided no sharp surge line but this is not a shortcoming of the results since in fact there is no sharp surge line. It is rather an area on the compressor map that tends to exhibit unstable behaviour. There are many factors influencing the actual stability limit: plenum volume, quality of inlet flow, fast or slow throttling, etc. Therefore, an accurate knowledge of the surge line alone will not allow to significantly reduce the surge margin for machines that are operated in a dynamic manner. In addition it needs surge control mechanisms that are able to inhibit this phenomenon – also if it occurs unexpectedly at an operational point that is considered to be stable.

Speed [rpm]	Critical throttle opening* [%]	φ_{crit} [—]	\dot{V}_{crit} [m ³ /s]
3000	5 ÷ 10	0.06 ÷ 0.11	0.116 ÷ 0.208
4000	5 ÷ 6	0.06 ÷ 0.07	0.155 ÷ 0.185
5000	6 ÷ 7	0.07 ÷ 0.08	0.230 ÷ 0.265

Table 7.1: Measured surge characteristics based on cross correlation; * orifice removed.

Speed [rpm]	Critical throttle opening* [%]	φ_{crit} [—]	\dot{V}_{crit} [m ³ /s]	$f_{surge,c}$ [Hz]	$f_{surge,p}$ [Hz]
3000	5 ÷ 10	0.06 ÷ 0.11	0.116 ÷ 0.208	7.9	6.8
4000	6 ÷ 7	0.07 ÷ 0.08	0.185 ÷ 0.213	7.3	6.8
5000	7 ÷ 8	0.08 ÷ 0.09	0.265 ÷ 0.296	6.8	6.6

Table 7.2: Measured surge characteristics based on spectra; * orifice removed.

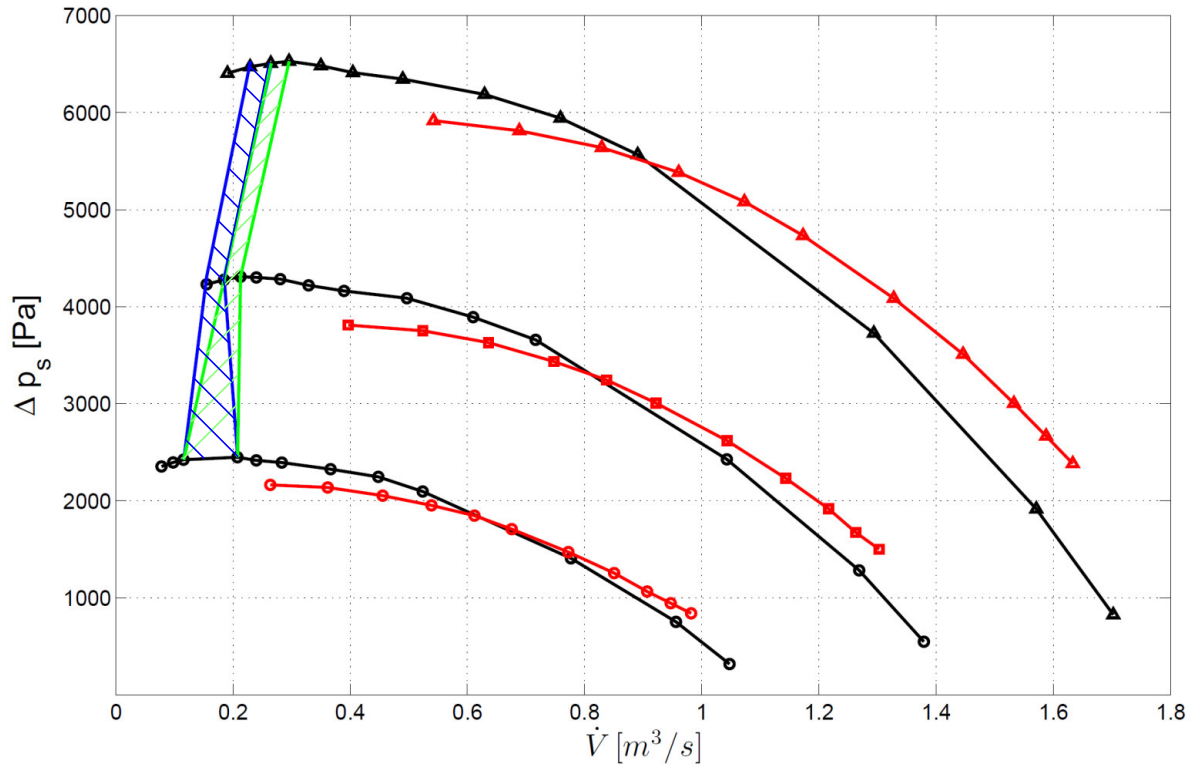


Figure 7.1: Surge line determined based on spectra (green) and cross correlation (blue), characteristics measured with fast (black) and slow (red) sensors.

Additionally an investigation on a simple model which correlates pressure fluctuations and turbulence intensity has been made. Unfortunately this model could not be supported by measurements. Nevertheless, turbulence intensity and the pressure RMS values showed similar trends at low mass flow rates.

Appendix A: Matlab Codes

Lumped Parameter Model

greitzer_dl.m

```
1 clear all; close all; clc;
2 %%%%%%%%%%%%%%%%%%%%%%%%%%%%%%%%%%%%%%%%%%%%%%%%%%%%%%%%%%%%%%%%%%%%%%%%%
3 global B G tau_dl Co_dl k_dl;
4 n=5000; % rotational speed [rpm]
5 R_2=0.2; % blade outlet radius [m]
6 N=0.5; % parameter [-]
7 L_C=7; % length of inlet duct [m]
8 L_T=3; % length of outlet duct
9 D_C=0.355; % diameter of inlet duct [m]
10 D_T=0.355; % diameter of outlet duct [m]
11 m_C_st=0.45; % initial mass flow [kg/s]
12 k_dl=1400; % dimensionless throttle coefficient [-]
13 rho=1.189; % density
14 V_P=0.3; % plenum volume
15 % coefficients of compressor characteritic representation
16 Co_dl=[-1873277.27048287 423849.351358882 -34283.0989392872
17         1137.98382216574 -13.1453086901828 0.998636212647166];
18 %%%%%%%%%%%%%%%%%%%%%%%%%%%%%%%%%%%%%%%%%%%%%%%%%%%%%%%%%%%%%%%%%%%%%%%%%
19 U=n/60*2*pi*R_2; % circumferential speed [rad/s]
20 A_C=D_C^2*pi/4; % cross sectional area inlet duct [m^2]
21 A_T=D_T^2*pi/4; % cross sectional area outlet duct [m^2]
22 omega=340*(A_C/(L_C*V_P))^0.5; % Helmholtz frequency [Hz]
23 B=U/(2*omega*L_C); % B parameter [-]
24 G=L_T*A_C/(L_C*A_T); % G parameter [-]
25 tau_dl=pi*R_2/L_C*(N/B); % dimensionless relaxation time [-]
26 m_C_st_dl=m_C_st/(rho*U*A_C); % dimensionless initial mass flow [-]
27 % dimensionless initial pressure rise
28 C_SS_start_dl=Co_dl(6)+m_C_st_dl*Co_dl(5)+m_C_st_dl^2*Co_dl(4)+m_C_st_dl^3*
29 Co_dl(3)+m_C_st_dl^4*Co_dl(2)+m_C_st_dl^5*Co_dl(1);
30 % solve
31 [t_dl,x_dl]=ode45(@greitzer_equations_dl,[0,1000],[m_C_st_dl,m_C_st_dl,
32 C_SS_start_dl,C_SS_start_dl]); % solve de
```

Listing 7.1: File for the Greitzer model simulation

greitzer_equations_dl.m

```

1 function xp = greitzer_equations_dl(t,sol)
2 %sol(1)=m_C_dl
3 %sol(2)=m_T_dl
4 %sol(3)=C_dl
5 %sol(4)=D_p_dl
6 global B G Co_dl tau_dl k_dl;
7 xp=zeros(4,1);
8 xp(1)=B*(-sol(4)+sol(3));
9 xp(2)=(B/G)*(sol(4)-k_dl*sol(2)^2);
10 xp(3)=1/tau_dl*(Co_dl(6)+sol(1)*Co_dl(5)+sol(1)^2*Co_dl(4)+sol(1)^3*Co_dl
    (3)+sol(1)^4*Co_dl(2)+sol(1)^5*Co_dl(1)-sol(3));
11 xp(4)=(1/B)*(sol(1)-sol(2));
12 end

```

Listing 7.2: File defining the equation system for the Greitzer model.

Compressor Map Measurement

SGP_map_1.m

```

1 clear all; close all; clc;
2 %%%%%%%%%%%%%%%%%%%%%%%%%%%%%%%%%%%%%%%%%%%%%%%%%%%%%%%%%%%%%%%%%%%%%%%%%
3 dB=0.211; % inner orifice diameter [m]
4 D=0.355; % inner duct diameter [m]
5 D3=0.350; % inner volute diameter at blower outlet [m]
6 D2=0.400; % outlet impeller diameter [m]
7 b2=0.024; % blade height at outlet [m]
8 fp={'15061501.txt' % file paths
9     '15061502.txt'
10    '15061503.txt'};
11 pU= repmat([98790 98840 98900],11,1); % ambient pressure [Pa]
12 hum=[0.66 0.68 0.68]; % humidity [-]
13 nu=[160.53*10^(-7) 159.865*10^(-7) 160.055*10^(-7)]; % kinematic viscosity
    [m^2/s]
14 cp=1007; % specific heat capacity [J/(kg K)]
15 kappa=1.4; % isentropic exponent [-]
16
17 % Pt100 calibration data
18 T0_kalib=[10 10; 13 13.1; 16 16.1; 19 19.1; 22 22.1; 25 25.2;
19           28 28.2; 31 31.2; 34 34.2];
20 T3_kalib=[10 9.9; 13 12.9; 16 15.9; 19 19.1; 22 22.1; 24.9 25.1;
21           28 28.2; 31 31.3; 34 34.3];
22 %%%%%%%%%%%%%%%%%%%%%%%%%%%%%%%%%%%%%%%%%%%%%%%%%%%%%%%%%%%%%%%%%%%%%%%%%
23
24 % initialize
25 M=zeros(11,13,3); T0=zeros(11,3); T3=zeros(11,3); pB1=zeros(11,3);
26 pB2=zeros(11,3); p0=zeros(11,3); p_sat0=zeros(11,3); p_sat3=zeros(11,3);
27 rho0=zeros(11,3); rho3=zeros(11,3); mdot=zeros(11,3); Vdot0=zeros(11,3);
28 Vdot3=zeros(11,3); cm0=zeros(11,3); cm2=zeros(11,2); cm3=zeros(11,3);

```

```

29 u2=zeros(11,3);p0t=zeros(11,3);p3t=zeros(11,3);psi_s=zeros(11,3);
30
31 % identify and calculate general data
32 for i=1:length(fp)
33     M(:, :, i)=dlmread(fp{i});
34     T0(:, i)=interp1(T0_kalib(:, 2), T0_kalib(:, 1), M(:, 6, i));
35     T3(:, i)=interp1(T3_kalib(:, 2), T3_kalib(:, 1), M(:, 7, i));
36     pB1(:, i)=pU(:, i)-M(:, 3, i);
37     pB2(:, i)=pB1(:, i)-M(:, 2, i);
38     p0(:, i)=pU(:, i)-M(:, 4, i);
39     p_sat0(:, i)=611.657*exp(17.2799-4102.99./(T0(:, i)+237.431));
40     p_sat3(:, i)=611.657*exp(17.2799-4102.99./(T3(:, i)+237.431));
41     rho0(:, i)=1./(8.314472*(T0(:, i)+273.15)).*(0.018*hum(i)*p_sat0(:, i)
        +0.02896*(p0(:, i)-hum(i)*p_sat0(:, i)));
42     rho3(:, i)=1./(8.314472*(T3(:, i)+273.15)).*(0.018*hum(i)*p_sat3(:, i)
        +0.02896*(pU(:, i)-hum(i)*p_sat3(:, i)));
43 end
44 A0=pi*D^2/4;A2=pi*D2*b2;A3=pi*D3^2/4; % calculate areas
45
46 for j=1:3 % calculate mass flow rate
47     for i=1:11
48         mdot(i, j)=orifice_flow_rate(dB,D,rho0(i, j),pB1(i, j),pB2(i, j),kappa,
            nu(j));
49     end
50 end
51
52 % calculate remaining values of interest
53 for i=1:3
54     Vdot0(:, i)=mdot(:, i)./rho0(:, i);
55     Vdot3(:, i)=mdot(:, i)./rho3(:, i);
56     cm0(:, i)=Vdot0(:, i)/A0;
57     cm2(:, i)=Vdot0(:, i)/A2;
58     cm3(:, i)=Vdot3(:, i)/A3;
59     u2(:, i)=D2*M(:, 8, i)*pi/60;
60     p0t(:, i)=p0(:, i)+rho0(:, i).*cm0(:, i).^2/2;
61     p3t(:, i)=pU(:, i)+rho3(:, i).*cm3(:, i).^2/2;
62     psi_s(:, i)=(p3t(:, i)-p0t(:, i))./(0.5*rho0(:, i).*u2(:, i).^2);
63 end
64 phi=cm2./u2;
65 pi_stat=pU./p0;
66 pi_tot=p3t./p0t;
67 delta_ht=(p3t-p0t)./rho0;
68 T0t=T0+1/cp*cm0.^2/2;

```

Listing 7.3: File for the data reduction of the compressor map measurement (orifice)

orifice_flow_rate.m

```

1 function [mdot]=orifice_flow_rate(d,D,rho1,pB1,pB2,kappa,nu)
2 % The function [mdot]=orifice_flow_rate(d,D,rho1,pB1,pB2,kappa,nu)
3 % calculates the mass flow rate according to DIN EN ISO 5167
4 %
5 % Input:
6 % d           : inner orifice diameter [m]
7 % D           : inner duct diameter [m]
8 % pB1         : overlap of windows (0.5=50%) [-]
9 % pB2         : cutoff frequency for low pass filter [Hz]
10 % kappa       : isentropic exponent [-]
11 % nu          : kinematic viscosity [m^2/s]
12 %
13 % Output:
14 % mdot        : mass flow rate [kg/s]
15
16 beta=d/D;
17 deltap=pB1-pB2;
18 epsilon1=1-(0.351+0.256*beta^4+0.93*beta^8)*(1-(pB2/pB1)^(1/kappa));
19 area=D^2*pi/4;
20
21 % solve equation system
22 options = optimset('TolFun', 1e-8,'TolX', 1e-8);
23 sol=fsolve(@equations,[0.1;10^5;0.01;100],options);
24 mdot=sol(1);
25
26 % definition of equation system
27 function ES = equations(sol)
28 ES(1)=sol(1)./(rho1*area)*D/nu-sol(2);
29 ES(2)=0.5961 + 0.0261*beta^2- 0.216*beta^8 + 0.000521*(10^6*beta/sol(2))
      ^0.7+(0.0188+0.0063*sol(3))*beta^3.5*(10^6/sol(2))^0.3-sol(4);%
      +0.043*(1-0.11*sol(3))*beta^4/(1-beta^4);
30 ES(3)=sol(4)*epsilon1*pi*d^2*(2*deltap*rho1)^0.5/(4*(1-beta^4)^0.5)-sol(1);
31 ES(4)=(19000*beta/sol(2))^0.8-sol(3);
32 end
33 end

```

Listing 7.4: File for the mass flow rate calculation (orifice)

SGP_map_2.m

```

1 clear all; close all; clc;
2 %%%%%%%%%%%%%%%%%%%%%%%%%%%%%%%%%%%%%%%%%%%%%%%%%%%%%%%%%%%%%%%%%%%%%%%%%%
3 ny=153.2*10^-7; % kinematic viscosity [m^2/s]
4 D_i=0.355; % inner diameter of inlet duct [m]
5 % filepath for 3000, 4000 and 5000 rpm
6 J_cta_3000={'Messdaten/cta/12041601_csv.txt'
7            'Messdaten/cta/12041602_csv.txt'
8            'Messdaten/cta/12041603_csv.txt'
9            'Messdaten/cta/12041604_csv.txt'
10           'Messdaten/cta/12041605_csv.txt'

```

```

11      'Messdaten/cta/12041606_csv.txt ',
12      'Messdaten/cta/12041607_csv.txt ',
13      'Messdaten/cta/12041608_csv.txt ',
14      'Messdaten/cta/12041609_csv.txt ',
15      'Messdaten/cta/12041610_csv.txt ',
16      'Messdaten/cta/12041611_csv.txt ',
17      'Messdaten/cta/12041612_csv.txt '};
18 J_cta_4000={'Messdaten/cta/12041613_csv.txt ',
19      'Messdaten/cta/12041614_csv.txt ',
20      'Messdaten/cta/12041615_csv.txt ',
21      'Messdaten/cta/12041616_csv.txt ',
22      'Messdaten/cta/12041617_csv.txt ',
23      'Messdaten/cta/12041618_csv.txt ',
24      'Messdaten/cta/12041619_csv.txt ',
25      'Messdaten/cta/12041620_csv.txt ',
26      'Messdaten/cta/12041621_csv.txt ',
27      'Messdaten/cta/12041622_csv.txt ',
28      'Messdaten/cta/12041623_csv.txt ',
29      'Messdaten/cta/12041624_csv.txt ',
30      'Messdaten/cta/12041625_csv.txt '};
31 J_cta_5000={'Messdaten/cta/12041627_csv.txt ',
32      'Messdaten/cta/12041628_csv.txt ',
33      'Messdaten/cta/12041629_csv.txt ',
34      'Messdaten/cta/12041630_csv.txt ',
35      'Messdaten/cta/12041631_csv.txt ',
36      'Messdaten/cta/12041632_csv.txt ',
37      'Messdaten/cta/12041633_csv.txt ',
38      'Messdaten/cta/12041634_csv.txt ',
39      'Messdaten/cta/12041635_csv.txt ',
40      'Messdaten/cta/12041636_csv.txt ',
41      'Messdaten/cta/12041637_csv.txt ',
42      'Messdaten/cta/12041638_csv.txt ',
43      'Messdaten/cta/12041639_csv.txt '};
44 J_edc_3000={'Messdaten/edc/12041601_edc.dat ',
45      'Messdaten/edc/12041602_edc.dat ',
46      'Messdaten/edc/12041603_edc.dat ',
47      'Messdaten/edc/12041604_edc.dat ',
48      'Messdaten/edc/12041605_edc.dat ',
49      'Messdaten/edc/12041606_edc.dat ',
50      'Messdaten/edc/12041607_edc.dat ',
51      'Messdaten/edc/12041608_edc.dat ',
52      'Messdaten/edc/12041609_edc.dat ',
53      'Messdaten/edc/12041610_edc.dat ',
54      'Messdaten/edc/12041611_edc.dat ',
55      'Messdaten/edc/12041612_edc.dat '};
56 J_edc_4000={'Messdaten/edc/12041613_edc.dat ',
57      'Messdaten/edc/12041614_edc.dat ',
58      'Messdaten/edc/12041615_edc.dat ',
59      'Messdaten/edc/12041616_edc.dat ',
60      'Messdaten/edc/12041617_edc.dat ',
61      'Messdaten/edc/12041618_edc.dat ',
62      'Messdaten/edc/12041619_edc.dat '

```

```

63     'Messdaten/edc/12041620_edc.dat ',
64     'Messdaten/edc/12041621_edc.dat ',
65     'Messdaten/edc/12041622_edc.dat ',
66     'Messdaten/edc/12041623_edc.dat ',
67     'Messdaten/edc/12041624_edc.dat ',
68     'Messdaten/edc/12041625_edc.dat '};
69 J_edc_5000={'Messdaten/edc/12041627_edc.dat ',
70     'Messdaten/edc/12041628_edc.dat ',
71     'Messdaten/edc/12041629_edc.dat ',
72     'Messdaten/edc/12041630_edc.dat ',
73     'Messdaten/edc/12041631_edc.dat ',
74     'Messdaten/edc/12041632_edc.dat ',
75     'Messdaten/edc/12041633_edc.dat ',
76     'Messdaten/edc/12041634_edc.dat ',
77     'Messdaten/edc/12041635_edc.dat ',
78     'Messdaten/edc/12041636_edc.dat ',
79     'Messdaten/edc/12041637_edc.dat ',
80     'Messdaten/edc/12041638_edc.dat ',
81     'Messdaten/edc/12041639_edc.dat '};
82 %%%%%%%%%%%%%%%%%%%%%%%%%%%%%%%%%%%%%%%%%%%%%%%%%%%%%%%%%%%%%%%%%%%%%%%%%
83 d1=max([length(J_cta_3000),length(J_cta_4000),length(J_cta_5000)]);
84 c_max=zeros(d1,3);p_m=zeros(d1,3);c_m=zeros(d1,3); % initialize
85 Re=zeros(d1,3);m=zeros(d1,3); % initialize
86 A=D_i^2*pi/4; % cross sectional area of inlet duct
87
88 % calculate mean pressures and central velocities
89 for i=1:length(J_cta_3000)
90     [~,~,c_max(i,1),~,~,~,~,~]=cta(J_cta_3000{i},1,0.5);
91     [~,~,p_m(i,1),~,~,~]=edc(J_edc_3000{i},1,0.5,200);
92 end
93 for i=1:length(J_cta_4000)
94     [~,~,c_max(i,2),~,~,~,~,~]=cta(J_cta_4000{i},1,0.5);
95     [~,~,p_m(i,2),~,~,~]=edc(J_edc_4000{i},1,0.5,200);
96 end
97 for i=1:length(J_cta_5000)
98     [~,~,c_max(i,3),~,~,~,~,~]=cta(J_cta_5000{i},1,0.5);
99     [~,~,p_m(i,3),~,~,~]=edc(J_edc_5000{i},1,0.5,200);
100 end
101
102 % calculate throughflow velocities based on power law
103 for i=1:3
104     for j=1:d1
105         [c_m(j,i),Re(j,i),m(j,i)]=m_interp(c_max(j,i),ny,D_i);
106     end
107 end
108
109 V=c_m*A; % calculate flow rates

```

Listing 7.5: File for the data reduction of the compressor map measurement

m_interp.m

```
1 function [c_m,Re,m]=m_interp(c_max,ny,L)
2 % The function [c_m,Re,m]=m_interp(c_max) calculates the throughflow
3 % velocity in a pipe based on the central velocity using a power-law
4 % assumption for the velocity distribution
5 %
6 % Input:
7 % c_max           : measured mean velocity in center of pipe [m/s]
8 % ny              : kinematic viscosity [m^2/s]
9 % L               : characteristic length [m]
10 %
11 % Output:
12 % c_m            : throughflow velocity [m/s]
13 % Re             : Reynolds number [-]
14 % m              : power law coefficient
15
16 delta=10^3; % start value
17 h=L/ny; % constant part of Re
18 Re2=c_max*h; % start value
19 m=0; % initialize power law coefficient
20 while delta>100 % interpolation for m
21     Re1=Re2;
22     if Re1<10^5&&Re1>4*10^3
23         m=6+1/96000*(Re1-4*10^3);
24     elseif Re1>10^5&&Re1<6*10^5
25         m=7+1/500000*(Re1-10^5);
26     end
27     c_m1=c_max*2*m^2/(2*m^2+3*m+1);
28     Re2=c_m1*h;
29     delta=abs(Re1-Re2); % checking termination condition
30 end
31 c_m=c_m1; % final value
32 Re=Re2; % final value
33 end
```

Listing 7.6: File for the interpolation of coefficient a for the throughflow velocity

Time Series Analysis

cta.m

```
1 function [fs,t,v_m,v_fl,f_ax_win,V_fl_w_avg,Tu,t_i,l_i]=cta(fp,K,ol)
2
3 % The function [fs,t,v_m,v_fl,f_ax_win,V_fl_w_avg,Tu,t_i,l_i]=cta(fp,K,ol)
4 % analyzes a time-resolved velocity measuring
5 %
6 % Input:
7 % fp           : filepath
8 % K            : number of windows in which the signal is divided [-]
9 % ol           : overlap of windows (0.5=50%) [-]
```

```

10 % fc_lp           : cutoff frequency for low pass filter [Hz]
11 %
12 % Output:
13 % fs             : sampling frequency [Hz]
14 % t              : time [s]
15 % v_m            : mean velocity [m/s]
16 % v_fl           : fluctuating velocity [m/s]
17 % f_ax_win       : frequency axis for single-sided spectrum [Hz]
18 % V_fl_w_avg     : double-sided spectrum of velocity values [m/s]
19 % Tu             : turbulence intensity [-]
20 % t_i            : integral time scale [s]
21 % l_i            : integral length scale [m]
22
23 % read data
24 fid0 = fopen(fp, 'r'); data=dlmread(fp, ','); fclose(fid0);
25
26 % identify data
27 t=data(:,1); % time [s]
28 v=data(:,2); % velocity [m/s]
29
30 N=length(t); % number of measured values
31 fs=N/ceil(max(t)); % sampling frequency
32
33 v_m=mean(v); % mean velocity [m/s]
34 v_fl=v-v_m; % fluctuating velocity vector [m/s]
35
36 N_w=floor(N/(0.5*K+0.5)); % number of values per window
37 v_fl_w=zeros(N_w,K); % initialize vector containing windows
38 v_fl_w(:,1)=v_fl(1:N_w); % first window
39 v_fl_w(:,end)=v_fl(end-N_w+1:end); % last window
40 j=0;
41 for i=1:(K-2)
42     v_fl_w(:,i)=v_fl(j:(j+N_w-1)); % remaining windows
43     j=j+ceil(N_w/2);
44 end;
45
46 func_w = repmat(hamming(N_w),1,K); % define window function
47 v_fl_fft = v_fl_w.*func_w; % apply window function on each window
48 NFFT_w = 2^nextpow2(N_w); % number of points for fft below
49 V_fl_w = fft(v_fl_fft,NFFT_w)./NFFT_w; % fast fourier transform
50 V_fl_w_avg=sum(abs(V_fl_w),2)/K; % average among windows
51
52 f_ax_win =0:fs/NFFT_w:fs/2; % corresponding frequency values [Hz]
53
54 % autocorrelation
55 acf=autocorr(v_fl, N-1, [], []);
56 for i=1:N
57     if acf(i)>0
58         continue
59     else
60         n=i;
61         break

```

```

62     end
63 end
64 t_i=1/fs*sum(acf(1:n)); % integral time scale [s]
65 l_i=t_i*v_m; % integrale length scale [m]
66 Tu=(sum(v_fl.^2)/N)^0.5/v_m; % turbulence intensity [-]
67 end

```

Listing 7.7: File for the data reduction of a velocity measurement

edc.m

```

1 function [fs,t,p_m,p_fl_fi_fi,f_ax_win,P_fl_w_avg]=edc(fp,K,ol,fc_lp)
2
3 % The function [fs,t,p_m,p_fl_fi_fi,f_ax_win,P_fl_w_avg]=edc(fp,K,ol,fc_lp)
4 % analyzes a time-resolved pressure measuring
5 %
6 % Input:
7 % fp           : filepath
8 % K           : number of windows in which the signal is divided [-]
9 % ol          : overlap of windows (0.5=50%) [-]
10 % fc_lp       : cutoff frequency for low pass filter [Hz]
11 %
12 % Output:
13 % fs          : sampling frequency [Hz]
14 % t           : time [s]
15 % p_m         : mean pressure [hPa]
16 % p_fl_fi_fi  : fluctuating press., stopband + lowpass filtered [hPa]
17 % f_ax_win    : frequency axis for single-sided spectrum [Hz]
18 % P_fl_w_avg  : double-sided spectrum of pressure values [hPa]
19
20 % read data
21 fid0 = fopen(fp,'r'); fid1 = fopen('helpdat.tmp','w');
22 fwrite(fid1, strrep(char(fread(fid0))',' ',' '.')); fclose(fid0);
23 fclose(fid1); Data = dlmread('helpdat.tmp'); delete 'helpdat.tmp';
24 t=Data(:,1); p=Data(:,2);
25
26 N=length(t); % number of measured values
27 fs=N/ceil(max(t)); % sampling frequency
28
29 p_m=mean(p); % mean pressure [hPa]
30 p_fl=p-p_m; % fluctuating pressure vector [hPa]
31
32 % filter parasitic frequency at 50Hz
33 wo = 50/(fs/2); % normalized frequency corresponding to 50Hz
34 q=25; % quality factor
35 bw = wo/q; % bandwidth at -3dB
36 [b,a] = iirnotch(wo,bw); % create a 2nd order iir notch filter
37 p_fl_fi=filter(b,a,p_fl); % filtered fluctuating pressure vector [hPa]
38
39 N_w=floor(N/(0.5*K+0.5)); % number of values per window
40 p_fl_w=zeros(N_w,K); % initialize vector containing windows
41 p_fl_w(:,1)=p_fl_fi(1:N_w); % first window

```



```

42 p_fl_w(:,end)=p_fl_fi(end-N_w+1:end); % last window
43 j=ol*N_w;
44 for i=1:(K-2)
45     p_fl_w(:,i)=p_fl_fi(j:(j+N_w-1)); % remaining windows
46     j=j+ceil(N_w/2);
47 end;
48
49 func_w = repmat(hamming(N_w),1,K); % define window function
50 p_fl_fft = p_fl_w.*func_w; % apply window function on each window
51 NFFT_w = 2^nextpow2(N_w); % number of points for fft below
52 P_fl_w = fft(p_fl_fft,NFFT_w)./NFFT_w; % fast fourier transform
53 P_fl_w_avg=sum(abs(P_fl_w),2)/K; % average among windows
54
55 f_ax_win =0:fs/NFFT_w:fs/2; % corresponding frequency values [Hz]
56
57 % filter high frequencies
58 [b,a]=butter(1, fc_lp*2/fs, 'low'); % 1st order Butterworth filter
59 p_fl_fi_fi = filter(b, a,p_fl_fi); % low pass filtered pressure signal
60 end

```

Listing 7.8: File for the data reduction of a pressure measurement

SGP_comb.m

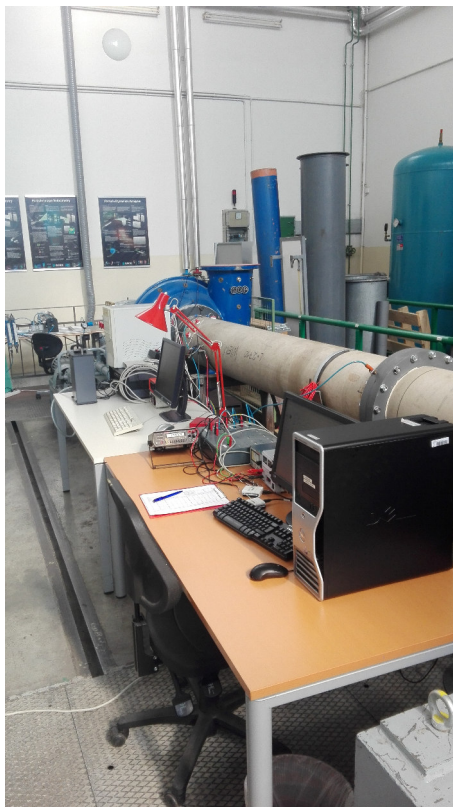
```

1 clear all; close all; clc;
2 %%%%%%%%%%%%%%%%%%%%%%%%%%%%%%%%%%%%%%%%%%%%%%%%%%%%%%%%%%%%%%%%%%%%%%%%%%
3 K=4; % number of windows in which the signals are divided
4 ol=0.5; % overlapping of windows (0.5=50%)
5 rho=1.25; % density [kg/m^3]
6 u2=104; % rotor tip speed [m/s]
7 fc_lp=15; % cutoff frequency for lowpass filtering of pressure signal [Hz]
8 max_per=10; % maximum expected period of pressure oscillation
9 filepath_cta='Messdaten/cta/12041639_csv.txt'; % path to velocity file
10 filepath_edc='Messdaten/edc/12041639_edc.dat'; % path to pressure file
11 %%%%%%%%%%%%%%%%%%%%%%%%%%%%%%%%%%%%%%%%%%%%%%%%%%%%%%%%%%%%%%%%%%%%%%%%%%
12
13 [fs,t,v_m,v_fl,f_ax_win,V_fl_w_avg,Tu,~,~]=cta(filepath_cta,K,ol);
14 [~,~,p_m,p_fl_fi_fi,~,P_fl_w_avg]=edc(filepath_edc,K,ol,fc_lp);
15
16 %%%%%%%%%%%%%%%%%%%%%%%%%%%%%%%%%%%%%%%%%%%%%%%%%%%%%%%%%%%%%%%%%%%%%%%%%%
17 % analysis of data correlation
18
19 [b,a]=butter(1, fc_lp*2/fs, 'low'); % 1st order Butterworth filter
20 v_fl_fi = filter(b, a,v_fl); % filtered velocity signal
21
22 % cross correlation
23 [r,lag] = xcorr(v_fl_fi,p_fl_fi_fi,max_per*fs,'coeff');
24 [~,I] = max(abs(r));
25 lagDiff = lag(I);
26 timeDiff = lagDiff/fs;

```

Listing 7.9: File for the correlation analysis of a velocity and a pressure measurement

Appendix B: Photographies





Bibliography

- [1] Bohl, W. , Elmendorf W. , *Strömungsmaschinen 1: Aufbau und Wirkungsweise*, 11th edition, Vogel Business Media (Kamprath-Reihe), 2012.
- [2] Bräunling, W.J.G. , *Flugzeugtriebwerke*, 4th edition, Springer-Verlag, Berlin Heidelberg, 2015.
- [3] Bruun, H. , H. , *Hot-Wire Anemometry – Principles and Signal Analysis*, Oxford University Press Inc. , New York 1995.
- [4] Cumpsty, N.A. , *Compressor Aerodynamics*, Longman Scientific & Technical , 1989.
- [5] Day, I.J. , *Stall, Surge, and 75 Years of Research*, Transactions of the ASME – Journal of Turbomachinery, Vol. 138, No. 1, January 2016, pp. 1-16.
- [6] Eckert, B. , Schnell, E. , *Axial- und Radialkompressoren*, 2nd edition, Springer-Verlag, Berlin Göttingen Heidelberg 1961.
- [7] Elder, R.L. , Gill, M.E. , *A Discussion of the Factors Affecting Surge in Centrifugal Compressors*, Transactions of the ASME – Journal of Engineering for Gas Turbines and Power, Vol. 107, No. 2, April 1985, pp. 499-506.
- [8] Hansen, K.E. , Jørgensen, P. , Larsen, P.S. , *Experimental and Theoretical Study of Surge in a Small Centrifugal Compressor*, Transactions of the ASME – Journal of Fluids Engineering, Vol. 103, No. 3, September 1981, pp. 391-395.
- [9] Greitzer, E.M. , *Surge and Rotating Stall in Axial Flow Compressors, Part I: Theoretical Compression System Model*, Transactions of the ASME – Journal of Engineering for Power, Vol. 98, April 1976, pp. 190-198.
- [10] Greitzer, E.M. , *The Stability of Pumping Systems*, Transactions of the ASME – Journal of Fluids Engineering, Vol. 103, No. 2, June 1981, pp. 193-242.
- [11] Krain, H. , *Review of Centrifugal Compressor's Application and Development*, Transactions of the ASME – Journal of Turbomachinery, Vol. 127, No. 1, January 2005, pp. 25-34.
- [12] Meulemann, C. Willems, F. , de Lange, R. , de Jager, B. , *Surge in a Low-Speed Radial Compressor*, ASME Paper 98-GT-426, Stockholm 1998.
- [13] Nitsche, W. , Brunn, A. , *Strömungsmesstechnik*, 2nd edition, Springer-Verlag, Berlin Heidelberg, 2006.

- [14] Pamphreen, R. C. , *Compressor Surge and Stall*, 1st edition, Concepts ETI, Inc. , Norwich, 1993.
- [15] Roth, H. , *Kennfeldmessung und strömungstechnische Nachrechnung eines Radialgebläses*, Diploma Thesis, Vienna University of Technology, 2014.
- [16] Siekmann, H. E. , Thamsen, P. U. , *Strömungslehre für den Maschinenbau*, 2nd edition, Springer-Verlag, Berlin Heidelberg, 2009.
- [17] Stenning, A. , H. , *Rotating Stall and Surge*, Transactions of the ASME – Journal of Fluids Engineering, Vol. 102, No. 1, pp.14-20, March 1980).
- [18] Willinger, R. , *The Cordier-diagram for compressors and fans*, VDI-Berichte, no.2112, 2010, pp. 17-28.